Non-equilibrium statistical physics of stochastic and chaotic Loewner evolutions

確率論的・カオス的レヴナー発展の非平衡統計物理学

Graduate School of Integrated Basic Sciences, Nihon University

日本大学大学院総合基礎科学研究科

Yusuke Shibasaki

柴﨑　雄介

This dissertation is based on and includes reuse and reproduction from

・Loewner driving force of the interface in the 2-dimensional Ising system as a chaotic dynamical system, Yusuke Shibasaki and Minoru Saito, *Chaos: An Interdisciplinary Journal of Nonlinear Science*, (2020) **30**(11), 113130, with the permission of AIP publishing.

・Permutation-Loewner entropy analysis for 2-dimensional Ising system interface, Yusuke Shibasaki *Physica A: Statistical Mechanics and its Applications*, (2022) **594**,126943.

・Fluctuation-dissipation theorem with Loewner time, Yusuke Shibasaki, *Europhysics Letters*. (2022) **139(**3), 31001.

and reference articles:

・Quantifying scaling exponents for neurite morphology of in vitro-cultured human iPSC derived neurons using discrete Loewner evolution: A statistical-physical approach to the neuropathology in Alzheimer's disease, Y. Shibasaki, N. Maeda, C. Oshimi, Y. Shirakawa, and M. Saito, *Chaos: An Interdisciplinary Journal of Nonlinear Science*, (2021) **31**(7), 073140.

Contents

1. Introduction — Loewner evolution and dynamical system 4

1.1 Loewner differential equation 5

1.2 Stochastic Loewner evolution 9

1.3 Chaotic Loewner evolution 13

2. 2D morphological analyses 18

2.1 Ising system 18

2.2 Neurite morphology 33

3. Loewner time 42

3.1 Concept of Loewner time 42

3.2 Fluctuation-dissipation relation 45

3.3 Application method 47

4. Conclusions 48

5. Acknowledgements 49

6. References 50

1. Introduction — Loewner evolution and dynamical systems

The Loewner evolution is a model of curve growth on the complex plane originally studied in the field of complex analyses [1-4]. The model is based on the Loewner differential equation suggested by Loewner in 1920s [1]. Its connections to mathematical and nonlinear physics have been well-developed since the discovery of stochastic Loewner evolution (SLE) by Schramm in 2000 [5, 6]. Combining the Loewner equation and methods of stochastic differential equation (SDE) yielded a one-parameter family of the conformal maps in the complex plane, which expresses conformally invariant random curves describing the geometry of the 2D statistical physical models [6, 7]. The efficacy of the SLE to analyze the geometries in the critical phenomena has been investigated in many literatures, using the stochastic analyses [7]. However, the clarification about its connection to the self-organization phenomena, e.g., diffusion-limited aggregation (DLA) [8-10], or Laplacian growth (LG) [10, 11], discussed in the field of nonlinear and non-equilibrium physics is still required. Here, I emphasize that the Loewner evolution is also discussed in the context of chaotic dynamical system theory because it is also considered as a dynamical evolution of time-dependent conformal map system. The purpose of this dissertation is to investigate the non-equilibrium physics of Loewner evolution, considering its chaotic properties and practical application methods. In this dissertation, I demonstrate the following results regarding the physical properties of Loewner evolution.

1. The discrete Loewner evolution has chaotic dynamical systems properties.

2. Practical applications of Loewner evolution to the 2D morphological data in the physical and biological systems.

3. The concept of Loewner time to analyze the one-dimensional non-equilibrium dynamics.

The remainder of this dissertation consists of the followings. In Sec. 1.1, I introduce the basic properties of chordal Loewner evolution, and in Sec. 1.2, I introduce the stochastic Loewner evolution (SLE) and its modified expressions that can be used in physics studies. In Sec 1.3, I introduce the

chaotic Loewner evolution as a possible generalization of the SLE and discuss its multifractal properties. Subsequently, in Sec. 2, I show the methods and results of the application of the discrete Loewner evolution to the 2D morphological data; the interfaces of the 2D Ising system (Sec. 2.1) and neurite morphology in *in vitro* cultured cells (Sec. 2.2). In Sec. 3, I discuss the concept of Loewner time, which is applicable to one-dimensional non-equilibrium dynamics for the future systematization of non-equilibrium physics of Loewner evolution. In Sec. 4, I remark the conclusions of the present work.

1.1 Loewner differential equation

In this subsection, I introduce the most familiar form of the Loewner differential equation, called the chordal Loenwer equation. The term *chordal* means that in this equation the curve takes a *cord-like* form. Let us consider the upper half complex plane denoted as $\mathbb{H}$ and the simple curve starting from the origin O parametrized by t as $\gamma_{[0,t]}$. The Riemann's mapping theorem ensures that there exists the conformal map from $\mathbb{H} \setminus \gamma_{[0,t]}$ to $\mathbb{H}$. Let us denote the sequence of such time-dependent conformal maps as $\{g_t\}$. The following Loewner equation determines a family of $g_t(z)$ $(z \in \mathbb{H})$ as [3-7]:

$$\frac{\partial g_t(z)}{\partial t} = \frac{2}{g_t(z) - \xi_t}, \quad g_0(z) = z \in \mathbb{H}. \tag{1.1.1}$$

Here, the term ξ_t is a one-dimensional and real-valued time function called driving function. In this form, the conformal map $g_t(z)$ is *hydrodynamically* normalized such that [3],

$$\lim_{z\to\infty} g_t(z) - z = 0. \tag{1.1.2}$$

In addition, $g_t(z)$ allows the power series expansion:

$$g_t(z) = z + \frac{2t}{z} + O(|z^{-2}|), \quad \text{as} \quad z \to \infty\,. \tag{1.1.3}$$

The relationship between the curve and driving function is expressed as

$$\lim_{z\to\gamma_t} g_t(z) = \xi_t. \tag{1.1.4}$$

This relation is obtained by the fact that conformal map $g_t(z)$ is not analytic when $z = \gamma_t$ because the dominator of the right-hand side of Eq. (1.1.1) becomes zero. The relation in Eq. (1.1.4) ensures the one-to-one correspondence of the coordinates of the curve $\gamma_{[0,t]}$ and driving function ξ_t, and is therefore often referred as the *encoding* (See, FIG.1 for the illustration of the mapping). In a practical sense, the determination of $\{g_t\}$ for an arbitrary curve or driving function is a difficult work, and it requires specific algorithms, one of which I shall introduce in the later subsection.

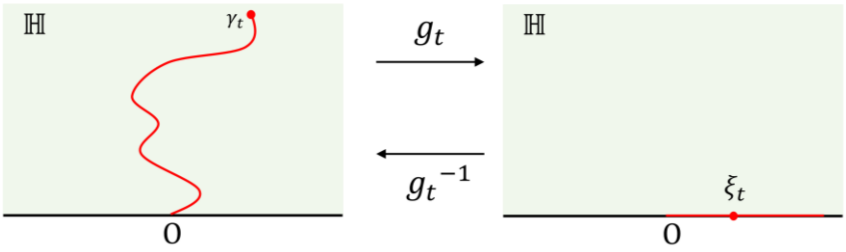

FIG. 1. Illustration of curve transformation of Loewner equation.

1.1.1 Composition property

In this subsection, I introduce the technical aspect of Loewner evolution based on Ref. 4. The sequence of $\{g_t\}$ that I have introduced is called the Loewner chain [3-7]. One of the important properties of g_t is the composition property. Let us consider the two conformal maps g_{t_A} and g_{t_B}. Here, g_{t_A} and g_{t_B} are generated by the Loewner equation in Eq. (1.1.1) whose driving function are ξ_t^A on the time interval $[0, t_A]$ and ξ_t^B on $[0, t_B]$, respectively. Then, let us define the following composite driving function [4]

$$\xi_t = \begin{cases} \xi_t^A & \text{for} \quad 0 < t < t_A \\ \xi_{t-t_A}^B & \text{for} \quad t_A < t < t_A + t_B \end{cases}. \tag{1.1.5}$$

For the Loewner chain $\{g_t\}$ the following composition rule can be applied. For the map g_t

generated by the composite driving function ξ_t in Eq. (1.1.5), the following relation holds [4].

$$g_{t_A+t_B}(z) = g_{t_B}\left(g_{t_A}(z)\right). \tag{1.1.6}$$

This property and Eq. (1.1.3) indicate that the mapping region $\mathbb{H} \setminus \gamma_{[0,t]}$ gets smaller as the time t gets larger. It means that the region $\gamma_{[0,t]}$ is larger than $\gamma_{[0,s]}$ if $t > s$ [4].

1.1.2 Discretization of the Loewner evolution and calculation algorithm

The discretized form of the chordal Loewner evolution was suggested in Ref 12. This treatment is important to implement the algorithm enabling the transformation from arbitrary curve-like data to the driving function and vise visa. In this subsection, I introduce the method called "zipper algorithm" using the vertical slit map [13-15]. Let us consider the following conformal map.

$$g_t(z) = \xi_t + \sqrt{(z-\xi_t)^2 + 4t}, \qquad z \in \mathbb{H}. \tag{1.1.7}$$

This is a solution of the Loewner equation and has a singular point at $z = \xi_t + 2i\sqrt{t}$. One can find that the map in Eq. (1.1.7) maps the vertical slit from $z = \xi_t$ to $z = \xi_t + 2i\sqrt{t}$ on $\mathbb{H}$ into the real axis and the tip of the slit moves to ξ_t [13-15] (See, FIG.2). To discretize the map g_t, we divide time t into the sequence of the reference point $\{t_n\}$ satisfying $t_0 = 0 < t_1 < t_2 < \cdots < t_n < \cdots < t_N$. Similarly, we denote the discretized points on the curve $\gamma_{[0,t]}$ as $\{z_0 = 0, z_1, z_2, \dots, z_n, \dots, z_N\}$. Then, we consider the "increments" of $g_t(z)$ in Eq. (1.1.7) as:

$$\tilde{g}_n \coloneqq g_{t_n} \circ {g_{t_{n-1}}}^{-1}. \tag{1.1.8}$$

For this definition and the composition property, $\tilde{g}_n(z)$ corresponds to each step of the map, which is divided from $g_{t_N}(z)$.

$$\tilde{g}_n(z) = \Delta\xi_{t_n} + \sqrt{(z-\Delta\xi_{t_n})^2 + 4\Delta t_n}. \tag{1.1.9}$$

Here, $\Delta\xi_{t_n} \coloneqq \xi_{t_n} - \xi_{t_{n-1}}$, and $\Delta t_n \coloneqq t_n - t_{n-1}$. Define the shifted map of $\tilde{g}_n(z)$ as;

$$h_n(z) \coloneqq \tilde{g}_n(z) - \Delta\xi_{t_n} = \sqrt{\left(z-\Delta\xi_{t_n}\right)^2 + 4\Delta t_n}. \tag{1.1.10}$$

Subsequently, define the map;

$$g_n(z) := \tilde{g}_n\left(z + \xi_{t_{n-1}}\right) - \xi_{t_{n-1}}. \tag{1.1.11}$$

Here, g_n is the solution of the Loewner equation with the driving function $\xi_{t_{n-1}+t} - \xi_{t_{n-1}}$, where t is a sufficiently small time interval. From Eqs. (1.1.9) to (1.1.11), the following relation is derived:

$$h_n \circ h_{n-1} \circ \cdots \circ h_1(z_n) = \tilde{g}_n \circ \cdots \circ \tilde{g}_1(z_n) - \xi_{t_n} = g_n(z_n) - \xi_{t_n} = 0. \tag{1.1.12}$$

If we stop the iterative transformation of h_n to z_n at $n-1$, we obtain the small vertical segment whose coordinate of the tip is denoted as w_n. For the above-mentioned property of the vertical slit, one can find that

$$w_n = \Delta\xi_{t_n} + 2i\sqrt{\Delta t_n}. \tag{1.1.13}$$

This relation means that if we obtain the sequence of $\{w_n\}$, we can extract the spatial and time increments of the driving function from the real and imaginary parts of w_n. To obtain w_n, we consider the following relationship,

$$w_n = h_{n-1} \circ h_{n-2} \circ \cdots \circ h_1(z_n), \qquad w_1 = z_1. \tag{1.1.14}$$

By applying this relation to the coordinates of the curve from $n = 1$ to $n = N$, the sequences of $\{\Delta\xi_{t_n}\}$ and $\{\Delta t_n\}$ are obtained. Then, summing up each sequence of the increments, the driving function is calculated from arbitrary discretized curve-like data [14]. In this dissertation, we use this algorithm to obtain the driving function corresponding to the real and theoretical data forming the curve-like morphology, e.g., interfaces of Ising system or neurite morphology.

Conversely, to obtain the curve-like coordinates from given 1D data of the driving functions, the following algorithm is available based the above discretization [15]. We deal with the case, where the unit time interval is a sufficiently small constant τ, satisfying $t = n\tau$. Then, the coordinate of the tip of the curve z_n is expressed as $z_n = {g_n}^{-1}(\xi_n)$. Dividing ${g_n}^{-1}$ into each step in a similar manner to that in Eq. (1.1.9), we obtain the following map [13],

$${\tilde{g}_n}^{-1}(z) = \Delta\xi_n + \sqrt{z^2 - 4\tau}\,. \tag{1.1.15}$$

Considering the relation in Eq. (1.1.12), nth coordinate of the curve z_n is expressed as,

$$z_n = {g_n}^{-1}(\xi_n) = {\tilde{g}_1}^{-1} \circ \cdots \circ {\tilde{g}_n}^{-1}(0)\,. \tag{1.1.16}$$

Using this relation, we can obtain the sequence of the coordinate of the curve $\{z_n\}_{n=0,1\ldots,N}$, which comprises discretized points on the curve $\gamma_{[0,t]}$, from arbitrary time series $\{\xi_n\}$ [13]. We shall use this algorithm to simulate the curve from the various types of the driving function to discuss its physical properties.

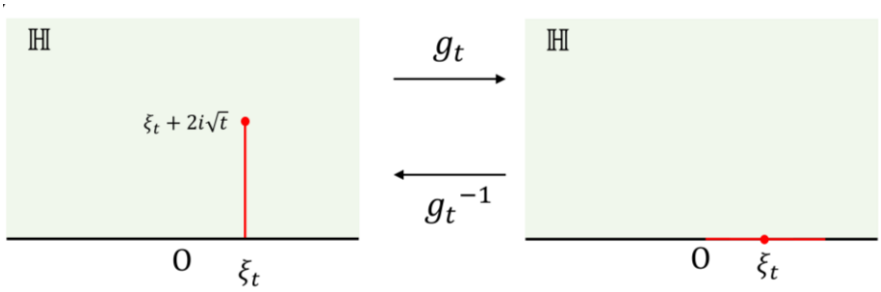

FIG. 2. Illustration of vertical slit map.

1.2 Stochastic Loewner evolution

The stochastic Loewner evolution suggested by Schramm takes a form of the combination of the Loewner evolution and Wiener process (standard Brownian motion) parametrized by a single diffusivity parameter, which is expressed as [3-7]:

$$\frac{\partial g_t(z)}{\partial t} = \frac{2}{g_t(z) - \sqrt{\kappa}B_t}, \qquad g_0(z) = z. \tag{1.2.1}$$

Here, κ is a diffusivity parameter and B_t is a standard Brownian motion. The SLE is suggested to explain the continuum limit of the conformally invariant geometry appearing in the 2D statistical physics models. The conformal invariance and scale invariance of the SLE curve are inherited from those of the standard Brownian motion. Equation (1.2.1) determines the one-parameter family of the conformal map $g_t(z)$, and the geometrical properties of the SLE curve are singly governed by κ. For example, the phases of the curve are determined depending on the diffusivity parameter κ, expressed

as follows [3, 4, 6, 7]:

・For $0 \leq \kappa < 4$, the SLE curve is a simple curve (i.e., it does not intersect itself).

・For $4 < \kappa < 8$, the SLE curve can intersect itself, but it is not space filling.

・For $\kappa \geq 8$, the SLE curve is a space filling curve.

These facts are derived by considering the Bessel process corresponding to the SLE in Eq. (1.2.1) and performing stochastic analyses [3]. Particularly, $\kappa = 4$ is a critical dimension of the Bessel process corresponding to the SLE. Another important quantity on the geometrical property of the SLE is the fractal dimension. For the latter discussions, I introduce the derivation process of the relation, which is described by Cardy [16]. Before discussing this matter, in the next subsection, we demonstrate another expression of the time evolution of the tip of the SLE curve using Langevin and Fokker-Planck equations [17, 18], frequently used equations in the context of non-equilibrium physics.

1.2.1 Fokker-Planck equation for SLE

Let us consider the backward flow of the chordal Loewner evolution, which is determined by the following equation ($w \in \mathbb{H}$) [6, 17, 18].

$$\frac{\partial f_t(w)}{\partial t} = -\frac{2}{f_t(w) - \xi_t}, \qquad f_0(w) = w. \tag{1.2.2}$$

It has been shown that $f_t(w)$ and ${g_t}^{-1}(w - \xi_t) + \xi_t$ have the same probability distribution (equal in distribution), if ξ_t satisfies the time-symmetric property and considered as a stationary increments process, e.g., Wiener process or Levy process, etc. Subsequently, considering $h_t \coloneqq g_t(z) - \xi_t$, it is found that the tip of the curve γ_t can be expressed as,

$$\gamma_t = \lim_{w \to 0} {h_t}^{-1}(w). \tag{1.2.3}$$

Defining $\tilde{z}_t \coloneqq f_t(w) - \xi_t$, it is found that $\tilde{z}_t$ and ${h_t}^{-1}(w)$ have the same probability distribution. We set $w = 0$ such that the temporal behavior of γ_t has same probability distribution as that of ${h_t}^{-1}(w)$. Then the differential equation that governs the behavior of $\tilde{z}_t$ is expressed as [17, 18]

$$\frac{\partial \tilde{z}_t}{\partial t} = -\frac{2}{\tilde{z}_t} - \frac{\partial \xi_t}{\partial t}. \tag{1.2.4}$$

Separating $\tilde{z}_t = u_t + iv_t$ into real and imaginary parts, we obtain the following 2-dimensional differential equation with random term. [17, 18]

$$\frac{\partial u_t}{\partial t} = -\frac{2u_t}{{u_t}^2 + {v_t}^2} - \frac{\partial \xi_t}{\partial t}\ , \tag{1.2.5}$$

$$\frac{\partial v_t}{\partial t} = \frac{2v_t}{{u_t}^2 + {v_t}^2}\ . \tag{1.2.6}$$

To make Eqs. (1.2.5) and (1.2.6) describe the dynamics of the tip of the curve, the initial conditions are set as $u_0 = 0$ and $v_0 = \varepsilon$, where ε is a positive infinitesimal constant. For the SLE case, we choose driving function as $\xi_t = \sqrt{\kappa}B_t$. In this case, the generalized Fokker-Planck equation corresponding to Eqs. (1.2.5) and (1.2.6) is expressed as follows [17]:

$$\frac{\partial p(u,v,t)}{\partial t} = \left(\frac{\kappa}{2}\frac{\partial^2}{\partial u^2} + \frac{\partial}{\partial u}\frac{2u}{u^2+v^2} - \frac{\partial}{\partial v}\frac{2v}{u^2+v^2}\right)p(u,v,t). \tag{1.2.7}$$

where, $p(u,v,t)$ is the probability distribution function of (u_t, v_t) defined as $p(u,v,t) := \langle \delta(u_t - u)\delta(v_t - v)\rangle$. These expressions facilitate the analyses of the dynamics of the SLE curve in the context of non-equilibrium physics, which will be demonstrated in Sec. 3.

1.2.2 Fractal dimension

The fractal dimension d_f of the SLE curve is expressed as:

$$d_f = 1 + \frac{\kappa}{8}, \quad \text{for} \quad d_f \leq 2. \tag{1.2.8}$$

Although there are several approaches to derive this relation, we introduce a method described by Cardy [16] for the latter discussions. The following definition of the fractal dimension is familiar to the physicists.

$$d_f = -\lim_{\varepsilon \to 0} \frac{\log N_\varepsilon}{\log \varepsilon}. \tag{1.2.9}$$

Here, ε is the radius of small discs centered at a point on the upper-half complex plane. N_ε denotes

the minimum number of small discs having radius ε required to cover the set of points comprising the SLE curve $\gamma_{[0,t]}$. Hereafter, we alter the definition of d_f in Eq. (1.2.9) into that involving the probability distribution function. First, we define $p(u,v,\varepsilon)$ as the probability distribution that a given point $u+iv$ exists within the distance ε from the SLE curve $\gamma_{[0,t]}$. It should be noted that if $p(u,v,\varepsilon) \sim \varepsilon^{\beta} p(u,v,\varepsilon)$ as $\varepsilon \to 0$ for a constant parameter β, the relationship $\beta = 2 - d_f$ holds true for the fractal dimension. Subsequently, let us consider the time evolution of $\gamma_{[0,t]}$ for an infinitesimal time dt. It indicates that the conformal map corresponding to dt is expressed as g_{dt}. For the scale invariance of the SLE curves, we assume that the measure of the curve is not varied under g_{dt}. It also means that $p(u,v,\varepsilon)$ satisfies the following [16, 18]:

$$p(u,v,\varepsilon) = p(u+du, v+dv, \varepsilon+d\varepsilon). \tag{1.2.10}$$

From Eq. (1.2.7), we obtain the relationships $du = \frac{2u}{u^2+v^2}dt$ and $dv = -\frac{2v}{u^2+v^2}dt$. Further, it has been shown that the radius ε is transformed as $\varepsilon \to |g'_{dt}(z)| \sim [1 - 2dt\mathrm{Re}(\frac{1}{z^2})]\,\varepsilon$ under g_{dt}. Using $du^2 = \frac{\kappa}{2}$ and performing Taylor expansion, we obtain the following [16, 18]

$$\begin{aligned} &p(u+du, v+dv, \varepsilon+d\varepsilon) \\ &\simeq p(u,v,\varepsilon) + \left[\frac{\kappa}{2}\frac{\partial^2}{\partial u^2} + \frac{2u}{u^2+v^2}\frac{\partial}{\partial u} - \frac{2v}{u^2+v^2}\frac{\partial}{\partial v} - 2\mathrm{Re}\left(\frac{1}{z^2}\right)\varepsilon\frac{\partial}{\partial \varepsilon}\right] p(u,v,\varepsilon)\,. \end{aligned} \tag{1.2.11}$$

Using Eq. (1.2.10) and expanding $\mathrm{Re}\left(\frac{1}{z^2}\right)$, Eq. (1.2.11) yields

$$\left[\frac{\kappa}{2}\frac{\partial^2}{\partial u^2} + \frac{2u}{u^2+v^2}\frac{\partial}{\partial u} - \frac{2v}{u^2+v^2}\frac{\partial}{\partial v} - \frac{2(u^2-v^2)}{(u^2+v^2)^2}\varepsilon\frac{\partial}{\partial \varepsilon}\right] p(u,v,\varepsilon) = 0\,. \tag{1.2.12}$$

Considering that $p(u,v,\varepsilon)$ should have the form of $\varepsilon^{2-d_f} \times (\text{a function of } u \text{ and } v)$, an ansatz that satisfies Eq. (1.2.12) has the following form [16, 18]:

$$p(u,v,\varepsilon) = \varepsilon^{2-d_f} v^A (u^2+v^2)^B\,. \tag{1.2.13}$$

Here, A and B are some constant parameters. Because $p(u,v,\varepsilon)$ is dimensionless, we obtain the following relationship:

$$A + 2B = d_f - 2\,. \tag{1.2.14}$$

Substituting Eq. (1.2.13) into Eq. (1.2.11), we obtain

$$A = \frac{(\kappa - 8)^2}{8\kappa}, \quad B = \frac{\kappa - 8}{2\kappa}. \tag{1.2.15}$$

From Eqs. (1.2.14) and (1.2.15), the fractal dimension d_f is expressed as

$$d_f = 1 + \frac{\kappa}{8}. \tag{1.2.16}$$

This result is valid for $d_f \leq 2$ [16].

The fractal dimension is frequently used quantity of the geometrical objects in the real-world data, and mainly discussed in the context of the dynamical system theory. An important property of the SLE is that the fractal dimension d_f is determined by the parameter κ of the driving function. It means that we can classify the complexity of SLE curve using a single parameter. However, most of the real-world data is not quantified by a single fractal dimension. Particularly, *multifractal* structures are often reported in biological and self-organization system. In the next subsection, I propose a possible generalization of the SLE using chaotic dynamical system.

1.3 Chaotic Loewner evolution

As a generalization of the SLE, I suggest the Loewner evolution driven by *chaotic* diffusion processes [18, 19]. Since 1990s, the Brownian motion driven by chaotic forcing has been studied by Shimizu, Beck, and Mackey [20-22]. Their studies were primary motivated by deterministic perspective for the random phenomena in physics based on the dynamical systems theory. One of the essential advantages for this perspective is the abundance of the chaotic dynamics, whose randomness is controlled by the bifurcation parameter. Using this property, I introduce the basic properties of the chaotic Loewner evolution and discuss its relation to the turbulent phenomena and self-organization systems.

1.3.1 Chaotic diffusion process as a driving function

As a driving function of the Loewner evolution, we construct a Wiener process-like diffusion process from a one-dimensional chaotic map. Let us consider the following logistic map [19];

$$x_{i+1} = 1 - ax_i^2, \qquad a \in [0, 2]. \tag{1.3.1}$$

Depending on the bifurcation parameter a the dynamics of $\{x_i\}$ qualitatively changes periodic one to chaotic random one. We here consider the chaotic region $a > 1.40115518909$ ..., where the central limit theorem is applicable in an approximate manner [23]. Let us define

$$\eta(x_i) = x_i - \bar{x}_i, \tag{1.3.2}$$

where $\bar{x}_i$ represents the time average calculated over all i. Subsequently, we consider the following diffusion process [19]:

$$V_t = \sqrt{\frac{\tau}{{\sigma_\infty}^2}} \sum_{i=1}^{n} \eta(x_i), \quad V_0 = 0. \tag{1.3.3}$$

Here, ${\sigma_\infty}^2 = \lim_{n\to\infty} {\sigma_t}^2$, where ${\sigma_t}^2$ is the variance of $\frac{1}{\sqrt{n}}\sum_{i=1}^{n}\eta(x_i)$. τ is a sufficiently small time interval satisfying $t = n\tau$. The variance ${\sigma_t}^2$ is expressed by the following autocorrelation function

$${\sigma_t}^2 = \langle \eta(x_0)^2 \rangle + 2\sum_{i=1}^{n} \langle \eta(x_0)\eta(x_i) \rangle. \tag{1.3.4}$$

For the central limit theorem for the mixing dynamical system, the correlation function (variance) in Eq. (1.3.4) converges in the limit of $t \to \infty$, that is

$$\lim_{t\to\infty} {\sigma_t}^2 = {\sigma_\infty}^2 (= const.). \tag{1.3.5}$$

For this fact, the diffusion process V_t is similar to the Wiener process B_t under the condition that the Markov approximation is valid. Then, we consider the chordal Loewner evolution driven by $\sqrt{\kappa}V_t$ as

$$\frac{\partial g_t(z)}{\partial t} = \frac{2}{g_t(z) - \sqrt{\kappa}V_t}, \qquad g_0(z) = z. \tag{1.3.6}$$

This is a model that I propose as a possible generalization of the SLE based on the deterministic

perspective. There is an important difference between V_t and B_t, which is derived from the essential property of the chaotic dynamics, that is, *decay of correlation* [24]. This property of the driving function V_t drastically changes the morphology and time evolution of the curve generated by the Loewner equation. FIG. 3 shows the example of the numerically simulated curves for $a = 1.7$ and usual SLE. Note that the driving function is the Wiener process parametrized by κ for the SLE, while ${\sigma_t}^2$ requires a certain length of time (denoted as t_c) to converges to a constant for the chaotic model with $a = 1.7$ [18, 19].

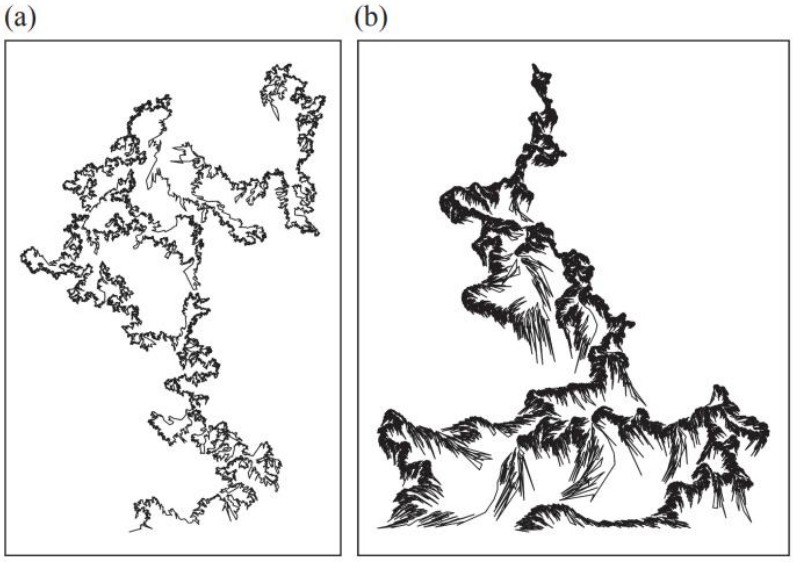

FIG. 3. Computed curve of SLE and chaotic Loewner evolution. Examples of (a) SLE for $\kappa = 6.0$. (b) chaotic Loewner evolution for $\kappa = 6.0$ and $a = 1.7$. (Referenced from Ref. 19)

1.3.2 Fokker-Planck equation for chaotic Loewner evolution

Using the studies by Shimizu and Beck [20, 21], the time evolution of the chaotic Loewner evolution described above is expressed by the Fokker-Planck equation similarly to that of the SLE. Let us define $\kappa' := \kappa/{\sigma_\infty}^2$, then the Fokker-Planck equation corresponding to the chaotic Loewner evolution in Eq. (1.3.6) is expressed as [18]

$$\frac{\partial p(u,v,t)}{\partial t} = \left\{\frac{\kappa'}{2}\left[\langle\eta(x_0)^2\rangle + 2\sum_{i=1}^{n}\langle\eta(x_0)\eta(x_i)\rangle\right]\frac{\partial^2}{\partial u^2} + \frac{\partial}{\partial u}\frac{2u}{u^2+v^2} - \frac{\partial}{\partial v}\frac{2v}{u^2+v^2}\right\}p(u,v,t). \tag{1.3.7}$$

The derivation process of this equation is similar to that described in Sec. 1.2.1. Practically, we shall use the Markov approximation of the chaotic dynamics to discuss its stochastic behavior.

1.3.3 Fractal property of chaotic Loewner evolution

The fractal dimension of chaotic Loewner evolution can be derived in a similar manner to that described in Sec. 1.2.2. We find that for a sufficiently long-time scale ($t > t_c$), the fractal dimension d_f is a constant value [18]:

$$d_f = 1 + \frac{\kappa'{\sigma_\infty}^2}{8} = 1 + \frac{\kappa'}{8}[\langle\eta(x_0)^2\rangle + 2\sum_{i=1}^{\infty}\langle\eta(x_0)\eta(x_i)\rangle]. \tag{1.3.8}$$

This result shows that the fractal dimension d_f of the curve can be expressed in terms of the correlation function of the employed chaotic maps of the driving function. It gives a slight but significant extension of the result of the SLE. If $\{\eta(x_i)\}$ does not have any autocorrelation ($a = 2.0$), this result can be simplified as [18]

$$d_f = 1 + \frac{\kappa'\langle\eta(x_0)^2\rangle}{8}, \tag{1.3.9}$$

and it is a constant independent of the time. In this case, the geometrical property of the curve is almost same as the SLE curve. The relations in Eq. (1.3.8) and (1.3.9) hold in $d_f \leq 2$.

1.3.4 As a model for self-organization and turbulence

We observed that the geometrical properties of the curves produced by chaotic Loewner evolution governed by the bifurcation parameter a of the logistic map. When the dynamics of the map satisfies is δ-correlated, the probabilistic behaviour of the tips of the curve is the same as that of the SLE by substituting $\kappa \to \kappa'{\sigma_t}^2$. In contrast, when the bifurcation parameter is set so that the dynamics of the

map have weak autocorrelations, the scale invariance of the curves is broken in $t < t_c$. In this situation, we observed the structure of the curves is locally aggregated, which is different from that of the SLE. This breaking of the fractality can be considered as an emergence of a kind of multi-fractal structure, which is known to be a common feature in self-organization. Consequently, we have shown that the time correlation in the driving force dominates such fractal properties of the curves, and it is related to the types and/or strength of the mixing property of the dynamics.

2. 2D morphological analyses

The theoretical scheme of the discrete Loewner evolution described in Sec. 1.1.2 is used to quantify the geometrical properties of 2D morphology in physical and biological system. The procedure of the analyses is described as the following. Step 1) Set the 2D curve-like morphology on upper half-plane $\mathbb{H}$. Step2) Compute the Loewner driving process. Step3) Apply time series analyses to the Loewner driving process. Hereafter, we show the results of the application of the above procedure to the physical and biological system, the interface of Ising system and neurite morphology, respectively. As a study of physics, it is important that obtained results are discussed in terms of their physical meanings. In such discussions, the Langevin and Fokker-Planck expressions described in Sec. 1.2.1 are useful.

2.1 Ising system

The geometry of interfaces, i.e., phase separation lines of two distinct phases, in the Ising system is a fundamental problem in statistical mechanics [25-29]. It is related to the basic physical properties of the system, such as the Hamiltonian or the configuration probability. Their complexity increases as the temperature T approaches the critical temperature T_c, and it has been indicated that the interface structures in the Ising system involve the local fluctuation explained by the central limit theorem (CLT). However, the exact mathematical description for these structures and its relation to the physical properties of the system itself have not been completely clarified.

In the context of the studies of SLE, the interface of the 2D Ising system at T_c is described by the SLE with $\kappa = 3$ in the continuum limit [30]. In the SLE theory, the local correlation and the scale invariance of the interfaces are explained using those of the Wiener process as a driving function. However, the SLE usually describes only the phenomena at T_c. wherein the system is conformally invariant. Therefore, it is necessary to extend the SLE framework using some approaches to describe those below T_c. While the SLE descriptions for such “off-critical” states have been investigated in

several studies [31-33], the common notion among them assumes that the off-critical states are induced by the autocorrelations in the driving forces of the Loewner evolution. It is also explained by the anomalous diffusion as a driving function [33].

2.1.1 Interface in the 2D Ising system

We consider the 2D ferromagnetic Ising model whose Hamiltonian is described as follows:

$$H = -\sum_{\langle i,j \rangle} \sigma_i \sigma_j . \tag{2.1.1}$$

Here, σ_i and σ_j are the nearest neighboring spins, which take the value of $\sigma_i \in \{-1, 1\}$ on the square lattice. At the critical temperature $T_c (= 2/\log(1+\sqrt{2}))$, the system undergoes a phase transition from an order to a disorder state. (Note that here T_c is rescaled by the Boltzmann constant.) To obtain the interfaces of the Ising model described by Eq. (1), the numerical simulations were performed using the Metropolis algorithm [34]. We chose 10 different values of T up to the critical temperature T_c; $T = 0.1\,T_c, 0.2\,T_c, \ldots, 1.0\,T_c$. Each numerical simulation was performed over 5×10^8 Monte Carlo steps, and we set the lattice size of 500×500 for all simulations. We employed a Dobrushin-type boundary condition; the nearest neighbors of the left half boundary were fixed as $\sigma_i = 1$, and those of the right half boundary as $\sigma_i = -1$. The interfaces that we shall analyze correspond to the lines passing between the center of the bottom side of the lattice (point A) and that of the upper side (point B) [FIG. 4(a)]. They can be uniquely defined so that they do not include any loops [28, 29]. The interfaces were extracted at the final states after 5×10^8 Monte Carlo steps. They were set on the upper half complex plane $\mathbb{H}$ so that a segment of the lattice is regarded as a unit square and point A corresponds to the origin. This transformation converts the interfaces to the curves $\gamma_{[0,t]} = \{z_0 = 0, z_1, z_2, \ldots, z_n, \ldots, z_N\}$ analyzed by the discrete chordal Loewner evolution. FIG. 4 shows an example of the spin configurations at $0.8\,T_c$ after 5.0×10^8 Monte Carlo steps [FIG. 4(a)], and the extracted interface on $\mathbb{H}$ [FIG. 4(b)].

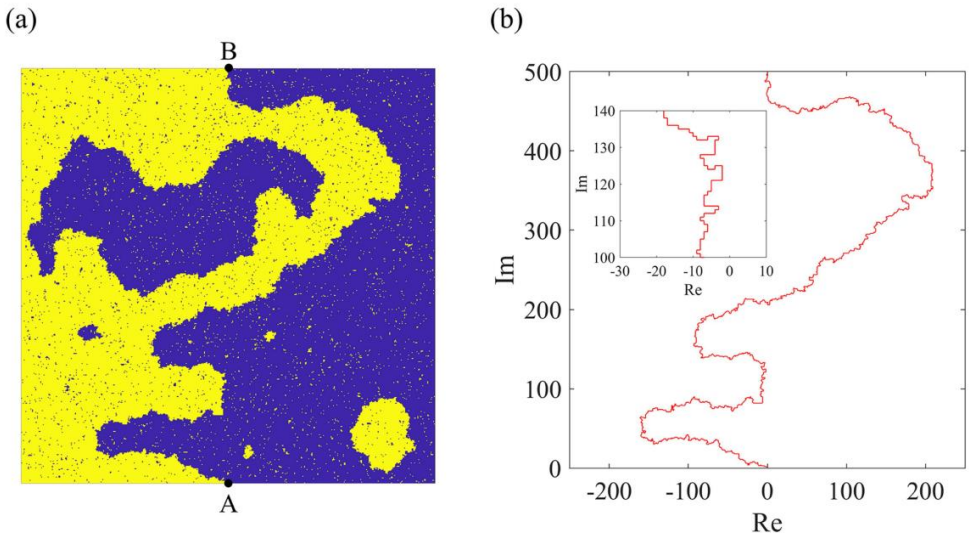

FIG. 4. Simulation result of the 2D Ising system. (a) Example of the spin configurations of the Ising system for $T = 0.8\,T_c$ after 5×10^8 Monte Carlo steps. The lattice size was set as 500×500. We employed a Dobrushin-type boundary condition; the nearest neighbors of the left half boundary were calculated as $\sigma_i = 1$, while those of the right half boundary as $\sigma_i = -1$. The yellow sites represent the spins of $\sigma_i = 1$, and the blue sites represent those of $\sigma_i = -1$. The center of the bottom side of the lattice and that of the upper side are denoted as points A and B, respectively. (b) Extracted interface for the spin configuration in (a). It was set on the upper half-plane $\mathbb{H}$ so that a segment of the lattice is regard as a unit square and point A corresponds to the origin. The inset displays an enlarged view of the interface.

2.1.2 Numerical calculation of Loewner driving function

The calculation of the Loewner driving function of the extracted curve $\gamma_{[0,t]} = \{z_0 = 0, z_1, z_2, \dots, z_n, \dots, z_N\}$ on $\mathbb{H}$ is performed using the algorithm in Sec. 1.1.2. Furthermore, we define the following variable referred to as the Loewner driving force:

$$x_n = \frac{\Delta\xi_{t_n}}{\sqrt{\Delta t_n}}, \quad x_0 = 0, \tag{2.1.2}$$

which is the main quantity of our analysis. Then, we define a random walk from the time-normalized driving force as follows:

$$y_n = \sum_{k=0}^{n} x_k . \tag{2.1.3}$$

For the SLE curves, the time series of $\{x_n\}$ should correspond to the white Gaussian noise, and $\{y_n\}$ should correspond to the Wiener process in the continuum limit.

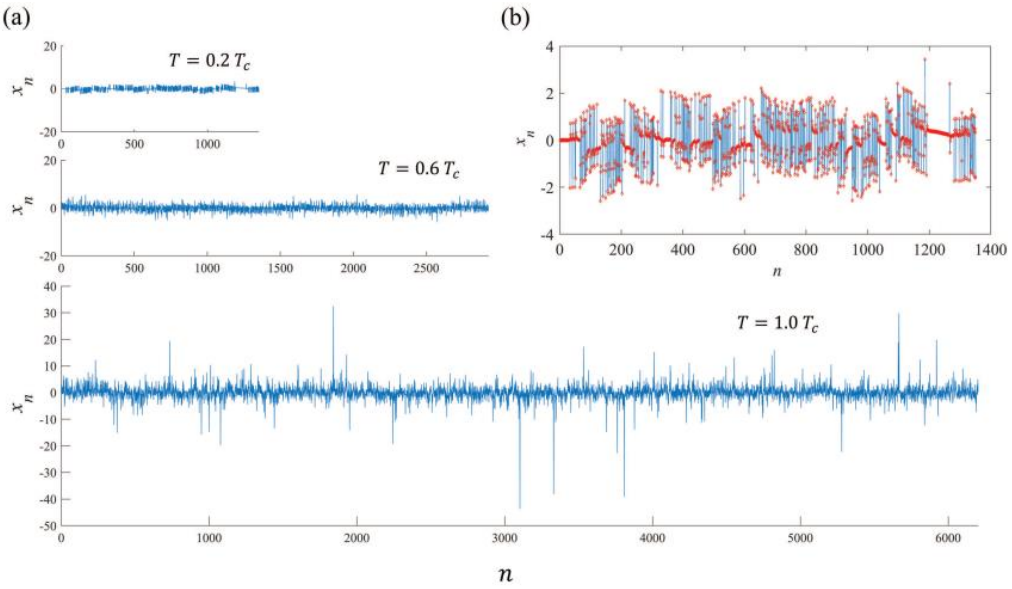

FIG. 5. Time series of the Loewner driving forces corresponding to the interfaces of the 2D Ising system. (a) Examples of the time series of $\{x_n\}$ for $T = 0.2\,T_c$, $0.6\,T_c$, and $1.0\,T_c$ from the top to bottom, respectively. Note that the data length and x_n-range increase as $T \longrightarrow T_c$. (b) Time series of $\{x_n\}$ for $T = 0.2\,T_c$ in an enlarged view. The red points and blue dotted lines display the data points and trajectories of the time series, respectively.

2.1.3 Intermittency and deterministic dynamics

We calculated the time series of $\{x_n\}$ corresponding to the Ising interfaces defined as $\gamma_{[0,N]}$ for 10 different temperatures; $T = 0.1\,T_c$, $0.2\,T_c, \ldots,$ $1.0\,T_c$. FIG. 5 shows examples of the time series for $T = 0.2\,T_c$, $0.6\,T_c$, and $1.0\,T_c$ from the top to bottom. Although the time series of $\{x_n\}$ showed random behaviors for all temperatures, we observed the on-off intermittency of the dynamics,

particularly at low temperatures [see the enlarged view for $T = 0.2\,T_c$ in FIG. 5(b)]. To evaluate this intermittency quantitatively, we employed the following algorithm modified from the interspike interval analysis [35, 36]: The indices of the time series of $\{x_n\}$ $(n = 0,1, \dots, N)$ are divided into $0 \leq L_0 < M_0 < L_1 < M_1 \cdots < L_k < M_k \cdots < L_m < M_m \leq N-1$, so that L_k and M_k are recursively determined to maximize $I_k = M_k - L_k$, satisfying the following:

$$\sum_{n=L_k}^{M_k} |x_{n+1} - x_n| \leq \Theta, \tag{2.1.4}$$

where Θ is a constant threshold value. Here, we fixed $L_0 = 0$ for the time series $\{x_n\}$ because $x_0 = 0$ and $x_1 = 0$ are valid for all of the time series that we analyze in this study. For this definition, I_k corresponds to the individual laminar phase length (off-state region), where the sum of the change in x_n is bounded by a threshold Θ. Using this method, we examined the intermittency of the Loewner driving force by computing the following quantities; a) the average length of the individual laminar phase length denoted as $\bar{I_k}\left(=\frac{1}{m+1}\sum_{k=0}^{m} I_k\right)$, and b) the ratio of the total length of the laminar phase to the total length of the time series denoted as $R(=\frac{1}{N}\sum_{k=0}^{m} I_k)$. FIG. 6(a) and 6(b) show the plots of $T\,/\,T_c$ and $\bar{I_k}$, and those of $T\,/\,T_c$ and R, respectively. Here, we chose $\Theta = 0.5$ and 1.0. In both figures, $\bar{I_k}$ and R take the largest value for $T = 0.2\,T_c$, and then they decreased as $T \longrightarrow T_c$. From these results, we found that the dynamics of the Loewner driving force has a temperature-dependent intermittency, which is most significant for $T \simeq 0.2\,T_c$.

As shown by Pommeau et al. [37], the intermittency of the dynamics is a crucial feature of the chaotic dynamical system. This implies that a deterministic mechanism underlies these dynamics. To confirm the existence of attractors for the dynamics of $\{x_n\}$, we analyzed the Poincaré plots for them. FIG. 7(a)-(c) show the Poincaré plots of x_n for $T = 0.2\,T_c$, $0.6\,T_c$, and $1.0\,T_c$, respectively. From these plots, we found that the dynamics of $\{x_n\}$ arises from some deterministic law, which should be more complicated than simple unimodal maps. In addition, the observed attractors have a nested

structure: the attractor of the low temperature is a part of that of the high temperature. The region of the attractor expands as $T \longrightarrow T_c$. It can be interpreted as a type of bifurcation.

To investigate the properties of these attractors quantitatively, we estimated Lyapunov exponents for the 2D time-delay embedding space defined as follows [38, 39]. Letting the initial separation vector of $X_n = (x_n, x_{n+1})$ as δX_0, the Lyapunov exponents $\Lambda = \{\lambda_1, \lambda_2\}$ $(\lambda_1 > \lambda_2)$ can be defined as

$$\Lambda = \lim_{N\to\infty} \frac{1}{N} \log\left|D_{X_0} F^N \delta X_0\right|, \tag{2.1.5}$$

where $D_{X_0}F$ represents the Jacobian matrix of the time evolution F of the trajectory of the system. For the numerical estimation of Λ, we used the algorithm of Eckmann et al [39]. FIG. 8 shows the obtained Lyapunov exponents for each $T\,/\,T_c$ (the upper for λ_1 and lower for λ_2). The largest exponent λ_1 for each temperature showed a positive value, which indicates the strong sensitivity to the initial conditions. Therefore, it was shown that the Loewner driving forces for all temperatures have a chaotic property. The qualitative change of their temporal behaviors is induced by expansion of the attractor, which depends on the temperature of the Ising system. From these results, we assume that the temperature-dependent route to chaos exists behind the Loewner driving forces of the 2D Ising interfaces.

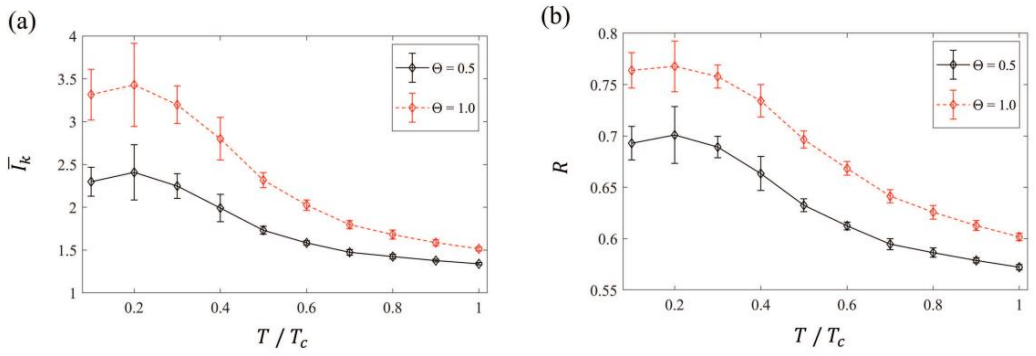

FIG. 6. Quantification of the intermittency of the Loewner driving force by the modified interspike interval analysis. (a) Plots of $T\,/\,T_c$ and $\bar{I}_k$ (the average length of the individual laminar phase length), (b) Plots of $T\,/\,T_c$ and R (the ratio of the total length of the laminar phase to the total length of the time

series). The black and red plots show those for $\Theta = 0.5$ and $\Theta = 1.0$, respectively. The markers in the plots show the average values calculated from 10 ensembles, and the error bars represent the standard deviations. In both figures, the intermittency of the dynamics of $\{x_n\}$ is found to be most remarkable for $T = 0.2\,T_c$, and decreases as $T \longrightarrow T_c$.

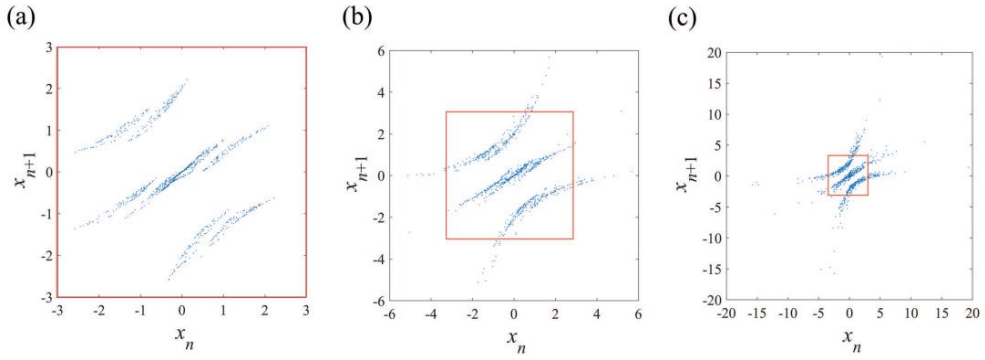

FIG. 7. Poincaré plots of Loewner driving force x_n, corresponding to the interfaces of the 2D Ising system. (a) $T = 0.2\,T_c$, (b) $T = 0.6\,T_c$, and (c) $T = 1.0\,T_c$. The attractors have a nested structure: the attractor of the low temperature is a part of that of the high temperature, and the region of the attractor expands as $T \to T_c$ [Compare the red squares in (b) and (c) with the attractor in (a)].

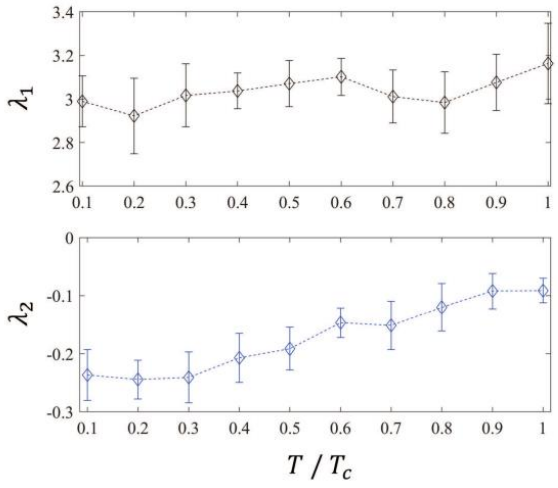

FIG. 8. Plots of $T\,/\,T_c$ and the estimated Lyapunov exponents for the 2D time-delay embedding space of $X_n = (x_n, x_{n+1})$ (the upper for λ_1 and lower for λ_2). The markers in the plots show the average values calculated from 10 ensembles, and the error bars represent the standard deviations. The largest exponent

λ_1 for each temperature showed a positive value, which indicates the strong sensitivity to the initial conditions.

2.1.4 Power spectral density

We have shown that the intermittent chaotic behaviors of $\{x_n\}$ depend on the temperature of the Ising system. To verify this route to chaos in more detail, however, we need to elucidate whether the dynamics of $\{x_n\}$ contains the specific periodic or quasiperiodic components. We examined the power spectral density (PSD) defined as

$$\mathrm{PSD}(\omega, x_n) = \frac{\Delta t}{N}\left|\sum_{n=0}^{N-1} e^{-in\omega} x_n\right|^2, \quad -1/2\Delta t < \omega \leq 1/2\Delta t, \tag{2.1.6}$$

where ω is a frequency and Δt is a sampling time interval, where we set $\Delta t = 1$. For the estimation of the PSD, we used the MATLAB signal processing toolbox pwelch function. FIG. 9(a) shows the plots of the calculated $\mathrm{PSD}(\omega, x_n)$ for $T = 0.2\,T_c$, $0.6\,T_c$, and $1.0\,T_c$ from the top to bottom, respectively. For $T = 0.2\,T_c$, where the dynamics has a significant intermittency as mentioned above, the $\mathrm{PSD}(\omega, x_n)$ includes several peaks although we cannot find any valid relationships, such as the period-doubling, among them. Contrarily, the spectra were broadened for $T = 0.6\,T_c$ and $1.0\,T_c$. These results indicate that the dynamics of $\{x_n\}$ becomes complicated as the system approaches the critical state although it may not correspond to the well-known routes to chaos. In addition, it was observed that the high-PSD part shifted from the high-frequency region to low-frequency region as $T \to T_c$. This suggests that the autocorrelation of $\{x_n\}$ also changes depending on the temperature of the system.

Subsequently, we examined the types of autocorrelations and scaling properties of the dynamics of the driving function, applying the PSD to $\{y_n\}$. FIG. 9(b) shows the log-log plots of ω and $\mathrm{PSD}(\omega, y_n)$ for $T = 0.2\,T_c$, $0.6\,T_c$, and $1.0\,T_c$. The linear decays of these plots indicate that the PSD

is scaled as $\mathrm{PSD}(\omega, y_n) \sim \omega^{-\beta}$, where β is a positive constant. It is known that $\beta = 2$ indicates that $\{y_n\}$ is an uncorrelated random walk, similar to the Wiener process [40, 41]. Although the log-log plots for the system below T_c showed slightly different scaling laws between the low- and high-frequency ranges, a good linearity was seen in the whole frequency range for $T = 1.0\,T_c$. This means that the scale invariance is the most valid for the critical temperature. FIG. 9(c) shows the relationship between $T\,/\,T_c$ and β approximated in the whole frequency range. We found that β becomes larger as $T \to T_c$, and they are ranged from $\beta = 1.38 \pm 0.07$ to 2.27 ± 0.02 (mean $\pm$ SD). Considering that $\beta = 1$ implies $1/f$ fluctuation, which is often caused by intermittent chaos [41], our numerical results suggest that $\{y_n\}$ is closer to $1/f$ noise at the lower temperatures. In addition, we obtained $\beta = 2.03 \pm 0.05$ for $T = 0.8\,T_c$, which indicates that $\{y_n\}$ is the closest to the uncorrelated random walk. It also means that the dynamics of $\{x_n\}$ below and above $T \simeq 0.8\,T_c$ have positive and negative autocorrelations, respectively. Thus, our results show that $\{x_n\}$ has some amount of autocorrelation even at $T = 1.0\,T_c$; in our numerical settings, the scaling of PSD indicates that the interface at $T \simeq 0.8\,T_c$ is closer to the SLE curve rather than that at $T = 1.0\,T_c$. Although this seems to contradict the theoretical results of the SLE, the same type of excessive correlation in the driving function has been also reported in Ref. 42, in which a similar numerical approach was adopted and it was interpreted as an effect of the finite size discretization.

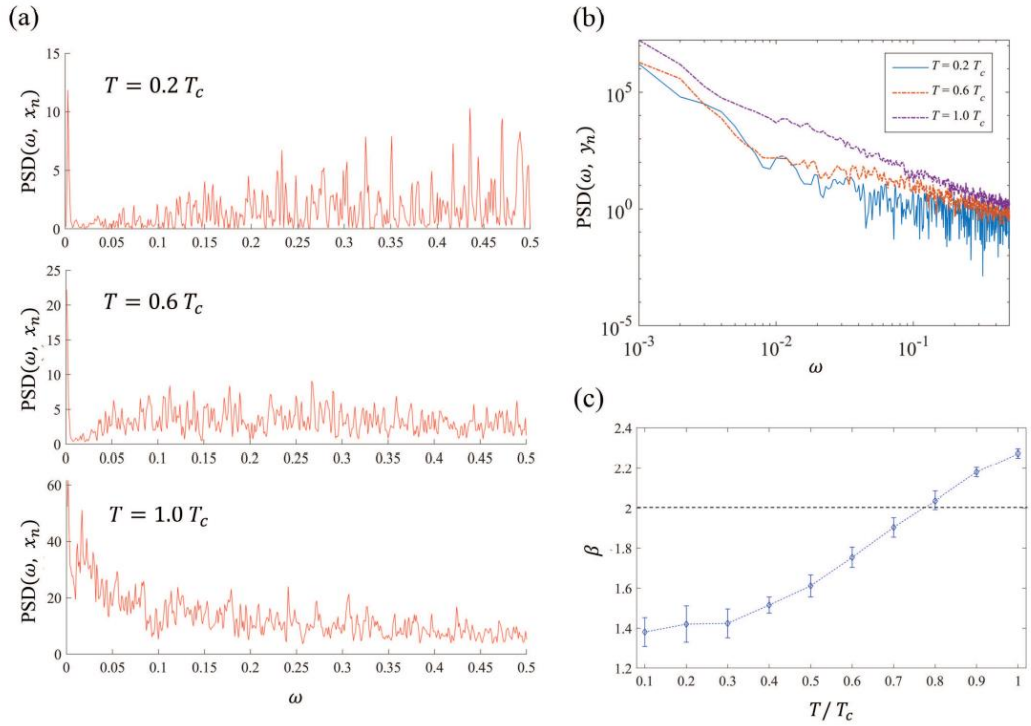

FIG. 9. Power spectral density (PSD) for the time series of $\{x_n\}$ and $\{y_n\}$. (a) PSD(ω, x_n) for $T = 0.2\ T_c$, $0.6\ T_c$, and $1.0\ T_c$ from the top to bottom, respectively. (b) Log-log plots of ω and PSD(ω, y_n) for $T = 0.2\ T_c$, $0.6\ T_c$, and $1.0\ T_c$. The approximated linear decays of these plots indicate that the PSD is scaled as PSD$(\omega, y_n) \sim \omega^{-\beta}$, where β is a positive constant. (c) The relation between $T\ /\ T_c$ and the average value of β approximated in the whole frequency range, calculated from 10 ensembles. The error bars represent the standard deviation. β becomes larger as $T \to T_c$, and ranges from $\beta = 1.38 \pm 0.07$ to 2.27 ± 0.02 (mean $\pm$ SD). In particular, we obtained $\beta = 2.03 \pm 0.05$ for $T = 0.8\ T_c$, which indicates that $\{y_n\}$ is close to the uncorrelated random walk.

2.1.5 Gaussian-type probability distributions

In the general arguments of the dynamical system theory, if the dynamics is chaotic, it should have invariant probability distribution determined by the invariant measure of the maps [38]. For the numerically calculated Loewner driving forces, the Gaussian-type probability distributions were

obtained. The probability distributions for $\{x_n\}$ were estimated using the MATLAB distribution fitter. FIG. 10(a) shows examples of the estimated probability distributions $P(x_n)$ for $T = 0.2\,T_c$, $0.4\,T_c$, $0.6\,T_c$, $0.8\,T_c$, and $1.0\,T_c$. The red lines in the plots show the fitted Gaussian curves. Although the chaotic maps that have Gaussian-type distribution have been reported in some literatures [43], it was found to be a notable character of the Loewner driving forces. In addition, it was observed that the variance κ of these distributions increased as $T \longrightarrow T_c$ [FIG. 10(b)]. Particularly, we obtained $\kappa = 6.36 \pm 0.53$ (mean $\pm$ SD) for $T = 1.0\,T_c$, which is consistent with the theoretical value of the percolation cluster [33, 42]. In addition, we obtained $\kappa = 2.96 \pm 0.31$ for $T = 0.8\,T_c$, which is the closest to theoretical value for the Ising system at the critical temperature [30]. The fitness to the Gaussian sharply decreased for $T = 0.9\,T_c$ and $1.0\,T_c$ [see, FIG. 10(c) for the log-likelihoods of the Gaussian fittings], which shows that the observed Gaussian distribution becomes distorted as $T \longrightarrow T_c$.

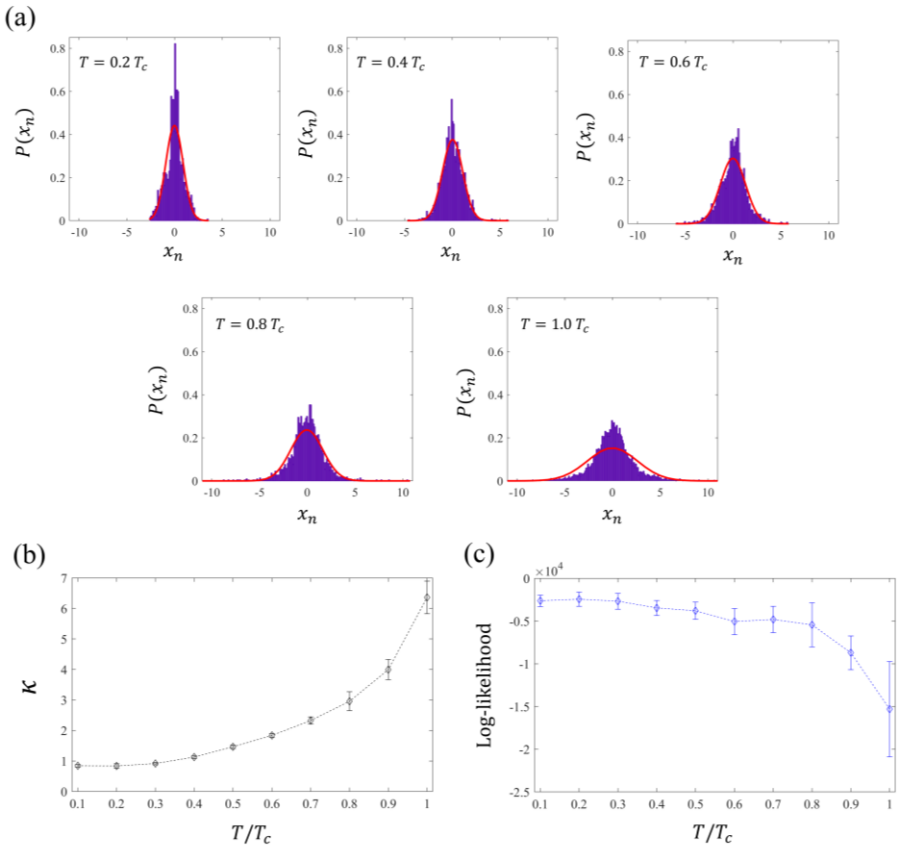

FIG. 10. Gaussian-type probability distributions of the Loewner driving forces. (a) Estimated probability distributions $P(x_n)$ of $\{x_n\}$ for $T = 0.2\,T_c$, $0.4\,T_c$, $0.6\,T_c$, $0.8\,T_c$, and $1.0\,T_c$. The red lines show the fitted Gaussian distributions. (b) Plot of $T\,/\,T_c$ and variance κ for $P(x_n)$, and (c) plot of $T\,/\,T_c$ and Log-likelihood of the Gaussian fitting. The markers in the plot show the average values calculated from 10 ensembles, and the error bars represent the standard deviation. At the critical temperature T_c, the variance takes $\kappa = 6.36 \pm 0.53$, which is consistent with the theoretical value of the percolation cluster. The fitness to the Gaussian sharply decreased for $T = 0.9\,T_c$ and $1.0\,T_c$.

2.1.6 Energy of the system and entropy of Loewner driving force

The entropy of the Loewner driving force works as a complexity measure for the geometry of the 2D Ising system. Let us define the following information entropy $S(x_n)$ for the Loewner driving

force x_n:

$$S(x_n) = -\sum_{x_n} p(x_n) \log p(x_n). \tag{2.1.7}$$

Here, $p(x_n)$ denotes the probability density function for x_n. In this subsection, we demonstrate a valid relationship between the above-defined Loewner entropy and the Hamiltonian H of the Ising system. The analog of the entropy in Eq. (2.1.7) for the time series $\{x_n\}$ was calculated using the permutation entropy method with 3! permutations (See Refs. 44 and 45 for details.) We refer to this entropy as permutation-Loewner entropy (PLE). FIG. 11 shows multiple plots of PLE and the mean energy per site H_{mean}, for $T/T_c = 0.05, 0.1, 0.15, \dots, 1.0$. We observed that PLE and H_{mean} exhibited an exponential relation. In the low-PLE region, we found that multiple temperatures were mixed to form a loosely rising curve. This indicates that the relationship between PLE and H_{mean} is independent of the temperature of the system. We estimated the function describing this relation using the curve-fitting toolbox in MATLAB [FIG. 11(b)]. The line plot in the FIG. 11(b) shows the function $y = ae^{bx} + ce^{dx}$, where $a = 0.00003014, b = 9.701, c = -1.971,$ and $d = -0.002808$. From this result, we conjecture that the Hamiltonian of the 2D Ising system can be expressed as a function of the information entropy $S(x_n)$ of the Loewner driving force, that is,

$$H = \sum_{k=1}^{m} a_k \exp\left[b_k S(x_n)\right], \tag{2.1.8}$$

where a_k, b_k and m are suitable constants.

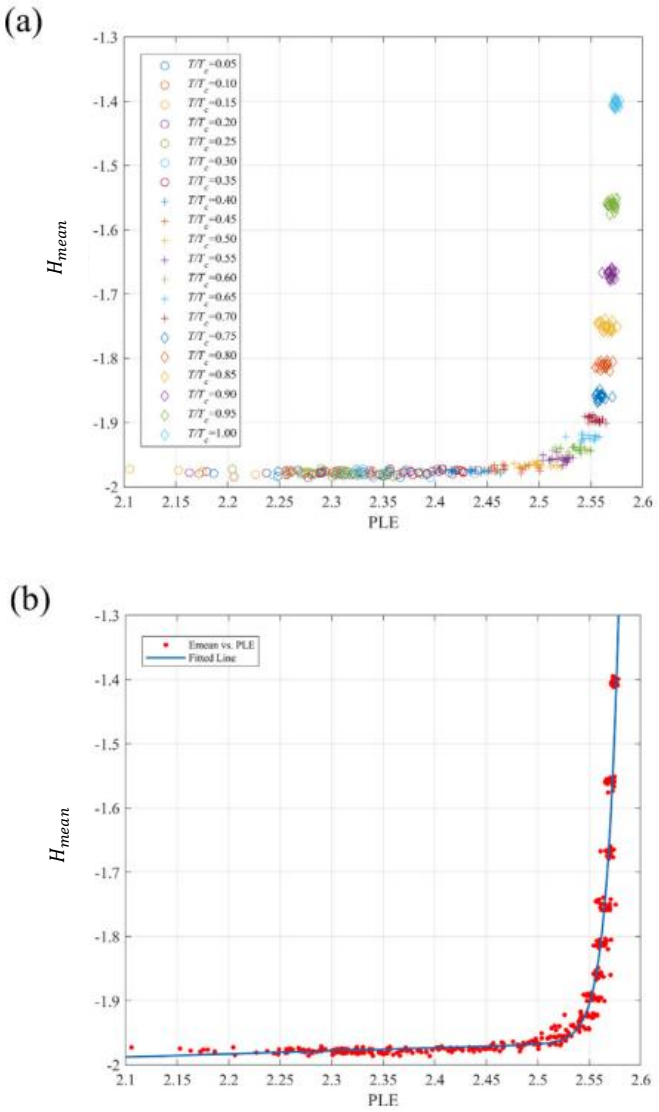

FIG. 11. Energy of the Ising system as a function of PLE. (a) Multiple plots of the PLE and mean energy per site H_{mean}, for $T/T_c = 0.05, 0.1, 0.15, \ldots, 1.0$. (b) Result of the exponential fitting for the plot in (a) approximated by the function $y = ae^{bx} + ce^{dx}$, where $a = 0.00003014, b = 9.701, c = -1.971,$ and $d = -0.002808$.

2.1.7 Discussion

From the results of the numerical analyses, the following conjectures about the Ising system and the Loewner driving forces can be made. 1) The Loewner driving forces, the normalized increments

of the driving functions, of the interfaces of the 2D Ising system each had a positive largest Lyapunov exponent and an attractor in the 2D time-delay embedding space. Therefore, the Ising interfaces are images of the *chaotic random walks* under the conformal transformations determined by discrete Loewner evolution. 2) The significant intermittency was observed in the dynamics of the Loewner driving forces of the Ising interfaces at the lower temperatures. This fact suggests that the autocorrelation in the Loewner driving forces in the 2D Ising system below T_c is induced by the intermittent chaotic property of the dynamics. 3) The qualitative change of the dynamics of the Loewner driving forces depended on the temperature of the 2D Ising system. Therefore, the bifurcation of the dynamics is dominated by the temperature of the system. 4) The probability distributions of the Loewner driving forces indicate that they are examples of *Gaussian chaos*. They become the closest to the white Gaussian noise at $T \simeq 0.8\,T_c$, but are deterministic. 5) In the framework of discrete Loewner evolution, the interfaces of the 2D Ising system at $T \simeq 0.8\,T_c$ have the statistical properties closest to those of the SLE curves. 6) The entropy of Loewner driving force determines the energy of the Ising system with an exponential function-type relation. It indicates that we can estimate fundamental physical property of the Ising system by the complexity of the 2D geometry.

Although we showed these properties of the Loewner driving forces by the numerical approach, we must remember that our analyses were based on a discrete-time version of the Loewner evolution. Therefore, we have to clarify how the observed chaotic scenario will behave in the continuum limit. However, based on the present results, an approach using chaotic dynamical systems to extend the SLE framework can be shown. A similar perspective to extend the SLE was suggested by the present authors before [18], in which the CLT for the chaotic driving dynamical systems [23] has a key factor of the behaviors of the systems. We expect that the previously indicated CLT [28, 29] for the interfaces of the 2D Ising system can be replaced by that for the chaotic driving forces, although this requires further investigations.

2.2 Neurite morphology

The variety of the morphology of individual neurons is one of the essential features of nervous systems, closely related to their functions and developments [46, 47]. Specifically, the morphological disorder of the neurites is a hallmark of the pathology of various neurodegenerative diseases. Alzheimer's disease (AD) is a typical example, in which the degeneration of neurites is considered as a key factor of its pathology. The main characteristics representing the abnormality in the AD neurons are dystrophic neurites (DNs) and neurofibrillary tangles (NFTs) [48-53]. The DNs exhibit disorders of the shapes of the axon and dendrite, having swollen and shrinking appearances induced by extracellular deposits of fibrillar β-amyloid (Aβ) called the plagues [49, 51, 52].

In most of the biological studies, however, the quantification method of the neurite morphology (including its disorder) has not been so valid, and the disorders such as DNs and NFTs are mainly evaluated by visual observations [49, 51, 52]. This fact means that there remains the ambiguity of the morphological definition of the neurite dystrophy, and diagnosing the neurodegenerative diseases solely based on morphological characteristics is still a difficult work for biological research. Although several mathematical and physical methods have been suggested to quantify the neurite morphology or neurite outgrowth (e.g., fractal dimensions [54], stochastic methods [55] or differential equations [56, 57]), quantifying the pathological state of the neurite morphology requires further improvements or alternatives of these models. Therefore, a systematic and theoretically plausible method to examine the degree of the morphological abnormality is needed to discuss the disordered state of morphology of nervous systems. This problem leads to the question about the physical interpretation of the neurite morphology and neurodegenerative disease. We approach this biological problem using the 2D morphological analyses using the Loewner evolution.

2.2.1 Culture of human induced pluripotent stem cell (iPSC)-derived neurons

The neural precursor cells derived from iPSC of the healthy person and AD patient were purchased from ReproCELL, Japan, ReproNeuro and ReproNeuro AD-patient-1, respectively. ReproNeuro AD-patient-1 was made from the AD patient whose Presenilin2 (PS2) gene includes the mutation (R62H). We performed the following procedure according to the protocol of ReproCELL. Before seeding, the culture dishes were first coated with the triple diluted 0.01% poly-l-lysine (PLL) solution for 2 hours, and subsequently coated with the coating solution diluted from ReproNeuro Coat (ReproCELL, Japan) overnight in the CO_2 incubator (37°C, 5%). The cells were seeded in the 12well culture plates with the density of 0.12×10^5 cells/cm^2 (the day in *vitro* 0 (DIV0)) and cultured in the CO_2 incubator at 37°C and 5% CO_2. The medium replacements were performed in DIV3 and DIV7. The culture medium (ReproNeuro Culture Medium, ReproCELL, Japan) for seeding and medium replacement was mixed with Additive A (ReproCELL, Japan), which promotes the differentiation of the cells to neurons. Thus, the iPSC-derived neural precursor cells have an ability to differentiate into neurons within 2 weeks. The cells have not completely differentiated in the earlier stages; however, we here refer to the cells as neurons.

2.2.2 Microscopic imaging and neurite tracing

The microscopic images of the iPSC-derived neurons were shot on DIV3, DIV5, DIV7, DIV10 and DIV14 with a phase-contrast microscope (CKX53, OLYMPUS). The digital images are obtained in 40 magnifications (FIG.12(a)). From the obtained images, we semi-automatically extracted the x-y coordinates of the neurites using Neuron J (a plugin for Image J), whose algorism is based on the second-order image derivative [58]. The parameters for the neurite tracing were set as follows; Hessian smoothing scale: 1.3, cost weight factor: 1.0, tracing smoothing range: 1, tracing subsampling factor:1 line width: 1. For this method, each neurite morphology was reduced to a set of the discretized points,

where 1 pixel of the digital image has length 1.0. The obtained neurite trace data were transformed into the upper half complex plane $\mathbb{H}$ so that the starting points of the neurite growth correspond to the origin O, and the coordinates of the real axis of the tips of the neurites is 0 (See, FIG.12(b)). We analyzed only neurites having forms of simple curves on $\mathbb{H}$, which do not intersect themselves and not extending beyond $\mathbb{H}$. As for the neurite having some branches, we choose only one path from the origin to tip per one cell to avoid the overlapping of the data. The number of neurite trace data we analyzed for each DIV was ranged from 534 to 834. The total number of neurites we analyzed through every DIV was 3055 for the healthy neurites and 4004 for the AD neurites, respectively.

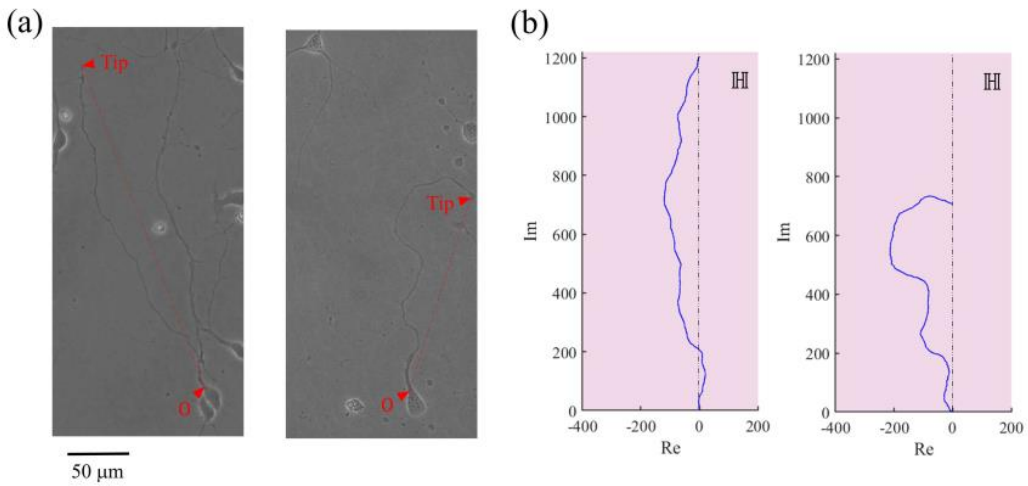

FIG. 12. The analytical procedure used in this study. (a) Examples of digital images of neurites taken on DIV5. The left image shows a healthy neurite (neurite A), and the right image shows an AD neurite (neurite B). (b) Neurite traces on the upper half complex plane $\mathbb{H}$ (left panel, neurite A; right panel, neurite B). The real (horizontal) and imaginary (vertical) axes are shown by "Re" and "Im", respectively. Each black dashed line shows the imaginary axis, which corresponds to the red dashed line in (a). One pixel of the digital image has a length of 1.0.

2.2.3 Detrended fluctuation analysis (DFA)

The time series of the Loewner driving force $\{x_n\}$ was numerically calculated for the neurite trace data. FIG. 13 (a) and (b) shows the Loewner driving force $\{x_n\}$ corresponding to neurite A and B, respectively. To examine the autocorrelations and scaling properties of the obtained time series of $\{x_n\}$, we performed the detrended fluctuation analysis (DFA) described as follows [59, 60]. Let us consider the following random walk-like path determined by x_n:

$$y(k) = \sum_{n=0}^{k} (x_n - x_{\mathrm{ave}}). \tag{2.2.1}$$

Here, x_{ave} is the time average of x_n over all n of the time series. Dividing the time series of $\{y(k)\}$ into the boxes of equal length s, we calculate the box size-dependent *trend* of $\{y(k)\}$ by calculating a linearly fitted segment line for the time series in each box. Let us denote $y_s(k)$ as the y-coordinate of the linearly fitted segment line, which represents the local trend. For the paths of $y(k)$, we can calculate the *detrended* fluctuation $F(s)$ as follows [59, 60]:

$$F(s) = \sqrt{\frac{1}{N}\sum_{k=1}^{N} [y(k) - y_s(k)]^2}. \tag{2.2.2}$$

Then, the autocorrelation and scaling property of the original time series $\{x_n\}$ can be examined by considering the following relationship:

$$F(s) \propto s^{\alpha}, \tag{2.2.3}$$

where α is the scaling exponent that determines the self-similarity of the time series. Practically, the slopes of the log-log plots of s and $F(s)$ were calculated to estimate the values of α. It has been shown that the time series are categorized into those having several types of autocorrelations depending on the values of α. For $\alpha \simeq 0.5$, $\{x_n\}$ is uncorrelated time series like the white Gaussian noise. For $\alpha > 0.5$, $\{x_n\}$ has a positive autocorrelation, and the correlation becomes larger as α gets apart from 0.5. Particularly, $\alpha \simeq 1.0$ indicates the well-known $1/f$ fluctuation. Contrarily, $\alpha < 0.5$ means an anti-correlation which also becomes larger as α gets apart from 0.5.

We performed the above-described DFA analysis to the time series $\{x_n\}$ corresponding to the neurite morphologies of the cultured neurons. FIG. 13(c) and 13(d) show the log-log plots of s and $F(s)$ for neurite A and neurite B, respectively. When the time series is short data set [61, 62], most of the obtained scaling exponents were different between the short-time and long-time ranges. This behavior is sometimes called the *crossover phenomena* [59]. We systematically estimate these two types of the scaling exponents by considering the local exponent $\alpha_L(s)$ defined as follows [61]:

$$\alpha_L(s) = \frac{\log F(s+1) - \log F(s)}{\log (s+1) - \log s}. \tag{2.2.4}$$

Subsequently, using MATLAB 'findchangepts' function, we detected one s-coordinate denoted as s_c, where the local exponent $\alpha_L(s)$ changes most drastically. The detections of the change point of the scaling exponent were performed in the range from $s = 10$ to $s = 100$, which was selected to be suitable for the data length of $\{x_n\}$. Then, we estimated the short-range and long-range exponents, α_1 and α_2, obtained by linear fittings for the ranges of $s = 3$ to $s = s_c$ and $s = s_c + 1$ to $s = N - 1$, respectively. The total scaling exponent, α_{tot}, for the total range ($s = 3$ to $s = N - 1$) was also calculated to observe overall tendency of the fluctuation. For the scaling exponents α_{tot}, α_1 and α_2, we examined their DIV-dependent behaviors (FIG. 14).

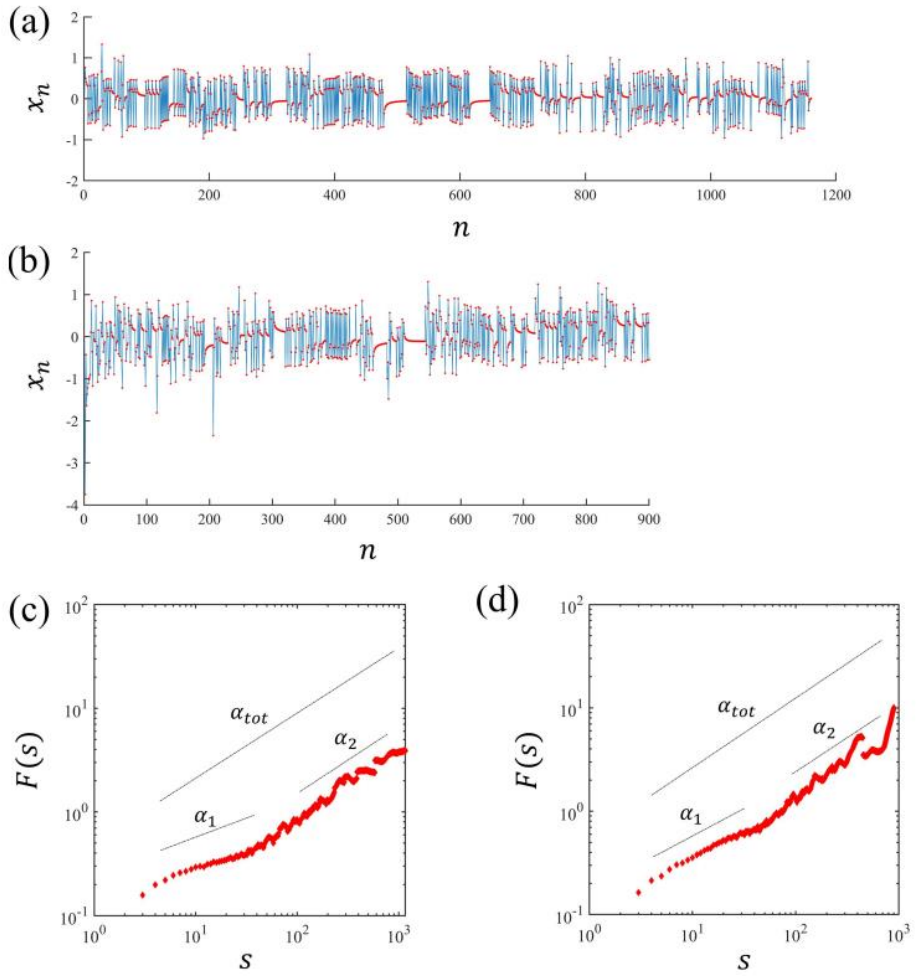

FIG. 13. Example of DFA. (a, b) Time series of the Loewner driving forces corresponding to (a) neurite A and (b) neurite B. (c, d) Log-log plots of s and $F(s)$ for (c) neurite A and (d) neurite B. The total, short-range, and long-range scaling exponents (α_{tot}, α_1, and α_2) are indicated in each graph. The corresponding values are $\alpha_{tot} = 0.63$, $\alpha_1 = 0.37$, and $\alpha_2 = 0.64$ for neurite A and $\alpha_{tot} = 0.67$, $\alpha_1 = 0.55$, and $\alpha_2 = 0.66$ for neurite B.

2.2.4 Statistical analysis

All data are expressed as means ± S.E.M (standard errors of means). For the scaling exponents obtained from 7059 samples of the neurite trace data (3055 for the healthy neurites and 4004 for the

AD neurites), we performed the two-way ANOVA (analysis of variance) to estimate the interactions of the factors of the cell type (healthy or AD) and DIV. After the ANOVA test, the *post-hoc* multiple comparison analyses were performed using Shaffer's modified sequentially rejective Bonferroni procedure to estimate the simple effect of the cell type on each DIV. These statistical analyses were performed with R software ver. 4.0.3. The significant difference of the ratio of each neurite type characterized by α_1 and α_2 between the healthy neurites and AD ones was verified by the χ^2-test. The critical *p*-value was set as 0.05 in these procedures.

2.2.5 Day *in vitro* (DIV)-dependent behavior of scaling exponents

We investigated the statistical properties of the quantified scaling exponents for each DIV and observed their DIV-dependent behaviors. FIG. 14(a)–(c) show α_{tot}, α_1 and α_2 at each DIV, where those for the healthy and AD neurites are shown as the blue and red plots, respectively. Evaluating by the differences from $\alpha = 0.5$, the DIV-dependent changes in α_{tot} and α_2 indicated that the healthy neurites have higher positive autocorrelations than the AD neurites during the earlier stages (DIV3–10), and these differences diminished as DIV increased. In contrast, the short-range exponent α_1 revealed the anti-correlations for both healthy and AD neurites at most DIV time points, where the correlations of the healthy neurites were higher than those of the AD neurites. In general terms, these results indicate that the healthy neurites have higher autocorrelations, that is, memory effects, than the AD neurites especially in the earlier stages (DIV3–10).

For α_{tot} and α_1, a two-way ANOVA showed that the interactions between the cell type and DIV has significant effects ($F_{(4,7049)} = 10.3465,\ p < 0.001$ for α_{tot}; $F_{(4,7049)} = 5.6778, p < 0.001$ for α_1). *Post-hoc* analyses revealed a significant simple effect of the cell type at each DIV, as shown in FIG. 14(a) and 14(b). Similarly, for α_2, a two-way ANOVA showed that the interaction between the cell type and DIV has a significant effect ($F_{(4,7049)} = 3.5395,\ p < 0.01$). *Post-hoc* analyses

revealed a significant effect of the cell type only from DIV3 to DIV10, as shown in FIG. 14(c). From these results, significant differences in the scaling exponents between the healthy neurites and AD neurites were identified, providing the statistical evidence that the healthy and AD neurites have different autocorrelative properties, particularly during the earlier stages of development (DIV3–10).

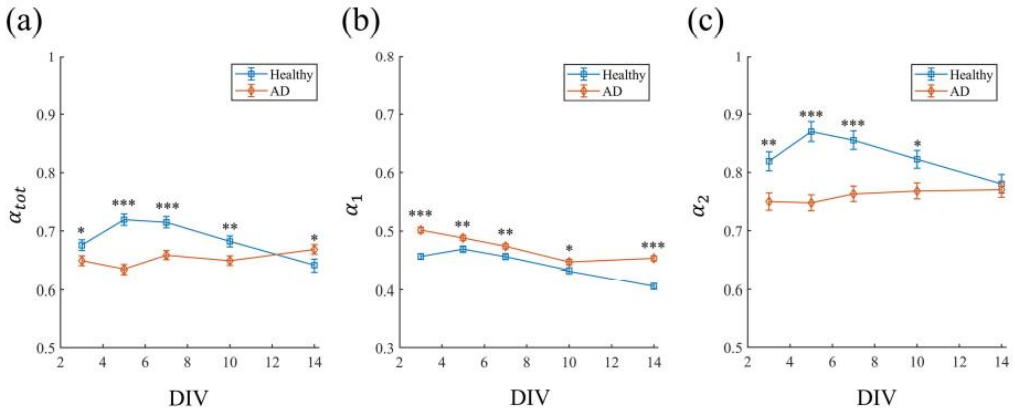

FIG. 14. Day in vitro (DIV)-dependent behaviors of the scaling exponents. (a) Plots of DIV versus the total scaling exponent α_{tot} for healthy (blue) and AD (red) neurites. (b) Plots of DIV versus the short-range scaling exponent α_1 for healthy (blue) and AD (red) neurites. (c) Plots of DIV versus the long-range scaling exponent α_2 for healthy (blue) and AD (red) neurites. Significant differences for each cell type (healthy or AD) on each DIV are indicated (*$p < 0.05$, **$p < 0.01$, ***$p < 0.001$). The data are expressed as the mean ± SEM.

2.2.6 Discussions

We investigated the early developments of the neurites of two types of iPSC-derived neurons, the healthy neuron and AD neuron, in terms of the scaling exponents for the corresponding Loewner driving forces. The differences in the scaling exponents between the healthy neurites and AD ones were significantly observed from DIV3. Especially, the long-range correlations in the morphology of the healthy neurites were higher than those of the AD ones in the earlier stages (DIV3-10). These

results can be interpreted that the AD neurites have a tendency of more random property than the healthy ones, and thus the AD neurites can be identified with loss of correlations, particularly for the long-range.

It is well-known that the meaning of the shapes in biology has been discussed by several theoretical biologist for decades [63-65]. Our method gives a physical interpretation for the biological morphology to answer the question; how much information a given biological shape has? In this view, our results lead to a physical hypothesis that *the neurodegenerative disease can be characterized by the neurite morphology having less information than that of the healthy state*. Further experimental verifications are required to validate this hypothesis.

3. Loewner time

3.1 Concept of Loewner time

The applications of the Loewner evolution described in the previous sections are intended to analyze the static 2D morphology of the physical and biological systems. In the analyses, the sequence of the time parameter of the Loewner driving force is obtained; however, physically it seems to have a dimension of space and its physical meaning is unclear. Mathematically, the time in the Loewner equation is defined as half plane capacity of the curve [3], and it is often referred to as the Loewner time. Therefore, to investigate the dynamical properties of Loewner evolution, which is important for the applications to the non-equilibrium physics [19, 66], we should clarify the relationship between the Loewner time and physical time in usual sense. A strategy that I suggest here is conversion method between Loewner time and physical time. The main idea described below is to regard the dynamics of Loewner evolution on the imaginary axis on the upper half-plane as physical time. I introduce an example of the applications to the anomalous diffusion process. Hereafter, we denote Loewner time as *s* and physical time *t*.

3.1.1 Time conversion to the anomalous diffusion

Consider the position of the particle $x(t)$ in a viscous fluid with a time evolution determined by the following nonlinear Langevin equation with a memory effect:

$$\frac{dx(t)}{dt} = F(\xi, t)\frac{d\xi(t)}{dt}, \tag{3.1.1}$$

where $\xi(t)$ denotes the position of the particle without memory effects, and its dynamics are determined by

$$\frac{d\xi(t)}{dt} = -\gamma\frac{\partial V[\xi(t)]}{\partial \xi} + \sqrt{2D}\eta(t). \tag{3.1.2}$$

Here, $V[\xi(t)]$ is a potential function of $\xi(t)$, γ is a damping constant, and D is the diffusion

constant. In Eq. (3.1.1), $\eta(t)$ is the white Gaussian noise with mean 0 and variance 1, which satisfies $\langle \eta(t)\eta(t') \rangle = \delta(t-t')$, where the brackets represent the ensemble average. $F(\xi,t)$ is a memory kernel expressed as

$$F(\xi,t) = f\frac{\xi(t)^2 + t^2}{t}, \tag{3.1.3}$$

where f is a constant parameter. Mathematically, Eqs. (3.1.1) and (3.1.2) belong to the class of stochastic differential equations (SDEs) describing the Ito diffusion [67]. For the effect of $F(\xi,t)$, the dynamics of $x(t)$ become non-Markovian and out-of-equilibrium. Specifically, this type of Langevin dynamics is considered to be equipped with multiplicative noise [68, 69] and a time-dependent drift term [69, 70]. [FIG. 15 shows the numerical simulation of an example of the dynamics of $x(t)$.]

Subsequently, let us consider the chordal Loewner evolution driven by $\xi(s)$ on the upper half-plane $\mathbb{H}$, which is expressed as [66]

$$\frac{\partial g_s(z)}{\partial s} = \frac{2}{g_s(z) - [\xi(s) - \xi(0)]}, \qquad g_0(z) = z \in \mathbb{H}, \tag{3.1.4}$$

where $g_s(z)$ is the Loewner map satisfying $g_s(z) = z + \frac{2s}{z} + O(z^{-2})$, which transforms the region $\mathbb{H} \setminus \lambda_{[0,s]}$ into $\mathbb{H}$. The Loewner equation in Eq. (3.1.4) describes the time evolution of the curve $\lambda_{[0,s]}$ starting at the origin. We impose the stationary condition from the initial state of the driving function $\xi(s)$. The formalism using the backward Loewner evolution shows that the time evolution of the tip of the curve $\lambda_s = \mathrm{Re}\lambda(s) + i\mathrm{Im}\lambda(s)$ has the same probability distribution as $z_s \coloneqq u(s) + iv(s)$ described by the two-dimensional Langevin equation: $\frac{du(s)}{ds} = -\frac{2u(s)}{u(s)^2+v(s)^2} - \frac{d\xi(s)}{ds}$ and $\frac{dv(s)}{ds} = \frac{2v(s)}{u(s)^2+v(s)^2}$[19, 66]. Here, the initial conditions are set as $u(0) = 0$ and $v(0) = \varepsilon$, where ε is a positive infinitesimal constant [19, 66]. Since $v(s)$ increases monotonically, we suppose that the imaginary part of the curve coordinate corresponds to time t. Through the transformation $v \to t$, the relationship between the time t and Loewner time s is expressed as

$$\frac{dt(s)}{ds} = \frac{2t(s)}{u(s)^2 + t(s)^2}, \tag{3.1.5}$$

where

$$\frac{du(s)}{ds} = -\frac{2u(s)}{u(s)^2 + t(s)^2} - \frac{d\xi(s)}{ds}. \tag{3.1.6}$$

For the above operation, $t(s)$ is transformed into a randomized time if we assume that s is a linearly increasing time variable. Using the Eqs. (3.1.1), (3.1.2), and (3.1.5), we found that the dynamics of $x(s)$ are governed by the following differential equation:

$$\begin{aligned}\frac{dx(s)}{ds} &= \frac{dx(t)}{dt}\frac{2t(s)}{u(s)^2 + t(s)^2} \\ &= f\frac{\xi^2 + t^2}{t}\frac{2t}{u(s)^2 + t^2}\left\{-\gamma\frac{\partial V[\xi(t(s))]}{\partial \xi} + \sqrt{2D}\eta(t(s))\right\}.\end{aligned} \tag{3.1.7}$$

In the limit of $s \to \infty$, the first term on the right-hand side of Eq. (3.1.6) vanishes and we obtain $\frac{du(s)}{ds} \backsimeq -\frac{d\xi(s)}{ds}$. Using the integral of this relation, Eq. (3.1.7) leads to

$$\frac{dx(s)}{ds} = -2f\left\{\gamma\frac{\partial V[x(s)]}{\partial x} - \sqrt{2D}\eta(s)\right\}, \qquad s \to \infty. \tag{3.1.8}$$

Consequently, we obtain a linear Langevin equation rescaled by the Loewner time s. It should be noted that the dynamics of $x(t)$ are converted into $x(s)$, which corresponds to those of the real part of the curve $\lambda_{[0,s]}$. This also means that the dynamics of $x(s)$ are similar to those of the driving function $\xi(s)$ in the long-time limit.

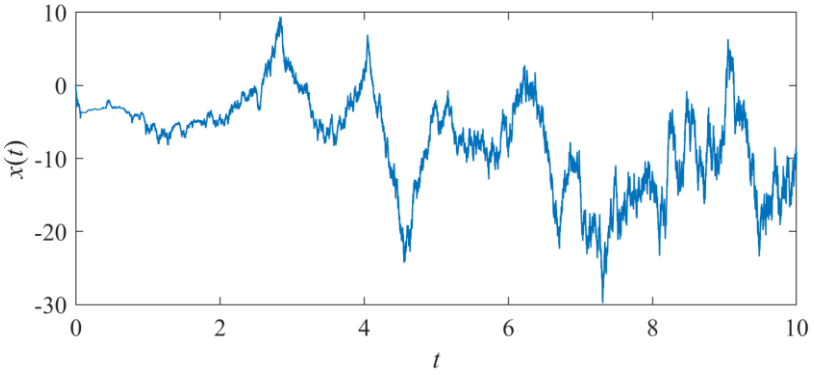

FIG. 15. Numerical simulation of the dynamics of $x(t)$. The potential function and parameters are chosen as $V[\xi(t)] = \frac{1}{2}\xi(t)^2$, $\gamma = 1.5$, $D = 2.0$, and $f = 1.0$. The time t is discretized as $t = n\tau$, where $\tau = 0.0001$.

3.2 Fluctuation-dissipation relation

The fluctuation-dissipation theorem can be immediately applied to $x(s)$ [or equivalently $\xi(s)$] in the following manner. (See, Ref. 71 for details.) Consider the correlation function $C(s,s') = \langle x(s)x(s')\rangle$, where $s > s'$. For the linear Langevin equation in Eq. (3.1.8), we obtain the following relationship: $\frac{\partial C(s,s')}{\partial s} - \frac{\partial C(s,s')}{\partial s'} = -4fD\phi(s,s')$ [71]. Assuming the equilibrium condition, the time-symmetric property of $x(s)$ yields $\frac{\partial C(s,s')}{\partial s} = -\frac{\partial C(s,s')}{\partial s'}$. Using these, we obtain the following linear response function:

$$\phi(s,s') = \frac{1}{2fD}\theta(s-s')\frac{\partial C(s,s')}{\partial s'}, \tag{3.2.1}$$

where $\theta(s-s')$ is the Heaviside step function [71]. Consequently, we demonstrated that the time coordinate change using the Loewner evolution enables us to analyze the response function $\phi(t,t')$ of the nonlinear Langevin equation in terms of the linear response function $\phi(s,s')$. The above formulation also holds for the class of nonlinear Langevin equations with $F(\xi,t) = ft + \sum_{n=0}^{m} f_n t^{-n}$, where f_n is the n-dependent coefficient, in the limit of $s \to \infty$ if the limit exists.

3.2.1 Estimation of nonlinear response

One of the advantages of the present approach is that it simplifies the mathematical expression of the nonlinear response function for the non-equilibrium dynamics. If the Loewner time coordinate change is successfully applied to non-equilibrium dynamics, the term describing the nonlinear response vanishes in $\phi(s,s')$ to be formalized by an equilibrium FDT. Furthermore, a new expression of nonlinear response function $\phi(t,t')$ is obtained by considering the transformation $\phi(s,s') \to \phi(t,t')$. For example, Eq. (3.2.1) is expressed as a nonlinear response function;

$$\phi(t,t') = \frac{1}{2fD}\theta(t-t')\left\langle \frac{2t'}{u^2+t'^2}x(s(t))\frac{d}{dt'}x(s'(t'))\right\rangle. \tag{3.2.2}$$

The capability of inverse transformation of time coordinate is guaranteed by the one-to-one correspondence between the curve and the driving function, including their distributions. It also implies that estimating the nonlinear response of non-equilibrium dynamics (in physical time) from the FDT in Loewner time is theoretically possible.

3.3 Application method

The time coordinate change using the Loewner time is expected to be applicable to experimentally obtained non-stationary dynamics. The key point of application method is that the sequence of the randomized time increments $\frac{dt(s)}{ds} \propto 1/\Delta s_n$ can be numerically obtained by the algorithm in Sec. 1.1.3. The practical application procedure of the proposed method to arbitrary non-equilibrium dynamics is described as follows: Step 1) For a given one-dimensional dynamics $\{x_n\}$, compose a sequence of complex-valued points $\{z_n\}$ on the curve $\lambda_{[0,s]}$ on $\mathbb{H}$, using the transformation $z_n = x_n + in$. $(n \geq 0, x_0 \equiv 0)$. Step 2) Compute the sequence of the time increments $\{\Delta s_n\}$ of the Loewner driving function ξ_s. Step 3) Multiply $\Delta x_n \coloneqq x_n - x_{n-1}$ and $1/\Delta s_n$ and integrate them to

obtain new dynamics $\{x_s\}$. Step 4) Estimate the probability distribution function (PDF) of $\{x_s\}$. If the PDF of $\{x_s\}$ converges to an invariant distribution and is close to that of the driving function $\{\xi_s\}$, it shows that the linear FDT with respect to the Loewner time s is valid. [See, FIG. 16(a) and (b) for the dynamics of x_s and Δs_n corresponding to $x(t)$ in FIG. 15, respectively. The estimated PDF of x_s is shown in FIG. 16(c)]. It also indicates that the laws in non-equilibrium dynamics x_n can be converted to those of the equilibrium driving function ξ_s. In Ref. 31, it was conjectured, under a certain condition, that if a random curve is described by a Loewner evolution, the driving function has the form of drift Brownian motion. Therefore, it should be emphasized that the validity of the Loewner time transformation in non-equilibrium systems is expected to be universal and reliable although further numerical and experimental examinations are required to be performed.

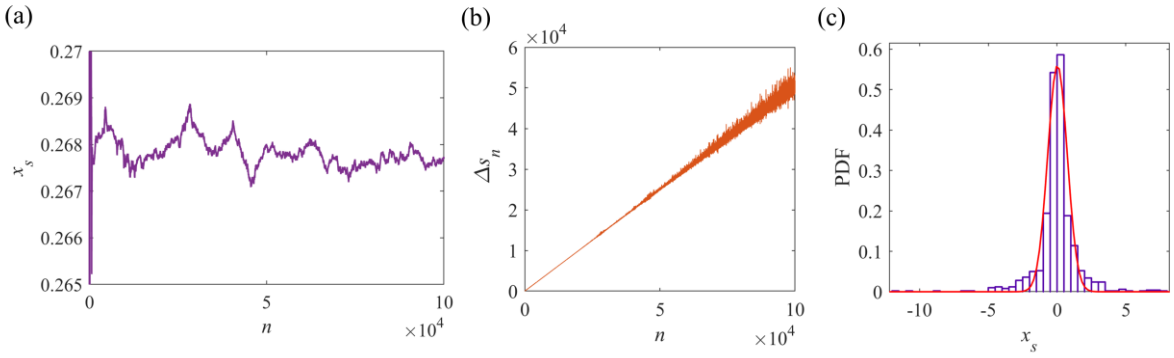

FIG. 16. Numerical results of the transformation using Loewner time. (a) Dynamics of x_s and (b) that of Δs_n, corresponding to $x(t)$ in FIG. 15. (c) Estimated PDF of x_s at $n = 1.0 \times 10^5$. The red-solid line shows the fitting line according to the Gaussian distribution.

4. Conclusions

We investigated the theory of the Loewner evolution in the context of chaotic dynamical system and non-equilibrium statistical physics. The dynamical laws in the Loewner evolution and SLE can be considered as a time (domain) -dependent conformal map system, which is different from the ordinary dynamical system. We demonstrated that the relationship between the curve on the complex plane and real-valued driving function is worth considering for both theoretical and application levels, indicating that it provides a novel perspective on the non-equilibrium physics. In this work, we focus on the phenomena that are not completely scale invariant (thus not conformally invariant), by expanding the SLE from a dynamical system point of view, which is not discussed enough in the previous studies. Especially, I remark that the theoretical scheme of the Loewner evolution also can be discussed with the contemporary information system theory, such as autopoietic theory [72]. Although the results of the present study should be updated such that it affords the systematization of the theory of non-equilibrium phenomena, its strategy will be based on the concept of the Loewner time transformation we discussed in Sec. 3. I hope that our results will provide an effective method to systematize non-equilibrium physics.

5. Acknowledgements

I would like to acknowledge Prof. Minoru Saito and Prof. Ken Judai for their supervising my research. I would like to also acknowledge Associate Prof. Daisuke Yamamoto for his helpful discussions. I also appreciate College of Humanities and Science and College of Art, Nihon University. I acknowledge Japan Society for the promotion of Science (JSPS No. JP20J20867) for the financial supports for this work.

6. References

1. Löwner, K. (Loewner, C.) (1923). Untersuchungen über schlichte konforme Abbildungen des Einheitskreises, I. *Mathematische Annalen* **89**,103-121.

2. Duren, P. L. Univalent Functions. (Springer-Verlag, New York, 1983).

3. Lawler, G. F. Conformally invariant processes in the plane. (American Mathematical Society, 2008)

4. Gruzberg, I. A., & Kadanoff, L. P. (2004). The Loewner equation: maps and shapes. *Journal of Statistical Physics*, **114**(5), 1183-1198.

5. Schramm, O. (2000). Scaling limits of loop-erased random walks and uniform spanning trees. *Israel Journal of Mathematics*, **118**(1), 221-288.

6. Rohde, S., & Schramm, O. (2005). Basic properties of SLE. *Annals of Mathematics*, **161**, 883-924.

7. Bauer, M., & Bernard, D. (2006). 2D growth processes: SLE and Loewner chains. *Physics Reports*, **432**(3-4), 115-221.

8. Witten T. A., & Sander, L. M. (1981). Diffusion-limited aggregation, a kinetic critical phenomenon. *Physical Review Letters*, **47**(19), 1400.

9. Witten, T. A., & Sander, L. M. (1983). Diffusion-limited aggregation. *Physical Review B*, **27**(9), 5686.

10. Barra, F., Davidovitch, B., Levermann, A., & Procaccia, I. (2001). Laplacian growth and diffusion limited aggregation: different universality classes. *Physical Review Letters*, **87**(13), 134501.

11. Feigenbaum, M. J., Procaccia, I., & Davidovich, B. (2001). Dynamics of finger formation in Laplacian growth without surface tension. *Journal of Statistical Physics*, **103**(5), 973-1007.

12. Bauer, R. O. (2003). Discrete Löwner evolution. *Annales de la Faculté des sciences de Toulouse: Mathématiques,* **12**(4), 433-451.

13. Kennedy, T. (2007). A fast algorithm for simulating the chordal Schramm–Loewner evolution. *Journal of Statistical Physics*, **128**(5), 1125-1137.

14. Kennedy, T. (2008). Computing the Loewner driving process of random curves in the half plane. *Journal of Statistical Physics*, **131**(5), 803-819.

15. Kennedy, T. (2009). Numerical computations for the Schramm-Loewner evolution. *Journal of Statistical Physics*, **137**(5), 839-856.

16. Cardy, J. (2005). SLE for theoretical physicists. *Annals of Physics*, **318**(1), 81-118.

17. Oikonomou, P., Rushkin, I., Gruzberg, I. A., & Kadanoff, L. P. (2008). Global properties of stochastic Loewner evolution driven by Lévy processes. *Journal of Statistical Mechanics: Theory and Experiment*, **2008**(01), P01019.

18. Shibasaki, Y., & Saito, M. (2020). Loewner evolution driven by one-dimensional chaotic maps. *Journal of the Physical Society of Japan*, **89**(5), 054801.

19. Shibasaki, Y., & Saito, M. (2020). Entropy flux in stochastic and chaotic Loewner evolutions. *Journal of the Physical Society of Japan*, **89**(11), 113801.

20. Shimizu, T. (1990). Relaxation and bifurcation in Brownian motion driven by a chaotic force. *Physica A: Statistical Mechanics and its Applications*, **164**(1), 123-146.

21. Beck, C. (1990). Brownian motion from deterministic dynamics. *Physica A: Statistical Mechanics and its Applications*, **169**(2), 324-336.

22. Mackey, M. C., & Tyran-Kamińska, M. (2006). Deterministic Brownian motion: The effects of perturbing a dynamical system by a chaotic semi-dynamical system. *Physics Reports*, **422**(5), 167-222.

23. Tirnakli, U., Beck, C., & Tsallis, C. (2007). Central limit behavior of deterministic dynamical systems. *Physical Review E*, **75**(4), 040106.

24. Henzel, H. P., & Ebeling, W. (1985). The decay of correlations in chaotic maps. *Physics Letters A*, **111**(1-2), 1-4.

25. Minlos R. A.& Sinaĭ. Ja G. (1967), The phenomenon of "phase separation" at low temperatures in some lattice models of a gas. I. *Mathematics of the USSR-Sbornik*, **2**(3), 335

26. Minlos, R. A. & Sinai, J. G. (1968) *Trans. Moscow Math. Soc.* **19**, 121.

27. Gallavotti, G. (1972). The phase separation line in the two-dimensional Ising model. *Communications in Mathematical Physics*, **27**(2), 103-136.

28. Bricmont, J., Lebowitz, J. L., & Pfister, C. E. (1981). On the local structure of the phase separation line in the two-dimensional Ising system. *Journal of Statistical Physics*, **26**(2), 313-332.

29. Akutsu, Y., & Akutsu, N. (1987). Intrinsic structure of the phase-separation line in the two-dimensional Ising model. *Journal of Physics A: Mathematical and General*, **20**(17), 5981.

30. Chelkak, D., Duminil-Copin, H., Hongler, C., Kemppainen, A., & Smirnov, S. (2014). Convergence of Ising interfaces to Schramm's SLE curves. *Comptes Rendus Mathematique*, **352**(2), 157-161.

31. Makarov, N. & Smirnov, S., "Off-critical lattice models and massive SLEs," in XVIth International Congress on Mathematical Physics (World Scientific, Singapore, 2010)

32. Kondo, Y., Mitarai, N., & Nakanishi, H. (2009). Loewner driving functions for off-critical percolation clusters. *Physical Review E*, **80**(5), 050102.

33. Credidio, H. F., Moreira, A. A., Herrmann, H. J., & Andrade Jr, J. S. (2016). Stochastic Loewner evolution relates anomalous diffusion and anisotropic percolation. *Physical Review E*, **93**(4), 042124.

34. Binder, K. & Heermann, D. W., Monte Carlo Simulation in Statistical Physics: An Introduction (Springer, New York, 2002)

35. Sauer, T. (1994). Reconstruction of dynamical systems from interspike intervals. *Physical Review Letters*, **72**(24), 3811.

36. Sauer, T. (1995). Interspike interval embedding of chaotic signals. *Chaos: An Interdisciplinary Journal of Nonlinear Science*, **5**(1), 127-132.

37. Pomeau, Y., & Manneville, P. (1980). Intermittent Transition to Turbulence in Dissipative Dynamical Systems. *Communications in Mathematical Physics*, **74**(2), 189-197.

38. Eckmann, J. P., & Ruelle, D. (1985). Ergodic theory of chaos and strange attractors. *Reviews of Modern Physics.* **57**, 617.

39. Eckmann, J. P., Kamphorst, S. O., Ruelle, D., & Ciliberto, S. (1986). Liapunov exponents from time series. *Physical Review A*, **34**(6), 4971.

40. Peng, C. K., Mietus, J., Hausdorff, J. M., Havlin, S., Stanley, H. E., & Goldberger, A. L. (1993). Long-range anticorrelations and non-Gaussian behavior of the heartbeat. *Physical Review Letters*, **70**(9), 1343.

41. Hausdorff, J. M., & Peng, C. K. (1996). Multiscaled randomness: A possible source of 1/f noise in biology. *Physical Review E*, **54**(2), 2154.

42. Stevenson, J. D., & Weigel, M. (2011). Percolation and Schramm–Loewner evolution in the 2D random-field Ising model. *Computer Physics Communications*, **182**(9), 1879-1882.

43. Eisencraft, M., Monteiro, L. H., & Soriano, D. C. (2017). White Gaussian chaos. *IEEE Communications Letters*, **21**(8), 1719-1722.

44. Bandt, C., & Pompe, B. (2002). Permutation entropy: a natural complexity measure for time series. *Physical Review Letters*, **88**(17), 174102.

45. Zanin, M., Zunino, L., Rosso, O. A., & Papo, D. (2012). Permutation entropy and its main biomedical and econophysics applications: a review. *Entropy*, **14**(8), 1553-1577.

46. S. Ramón y Cajal, J. DeFelipe, & E. G. Jones, Cajal's Degeneration and Regeneration of the Nervous System (Oxford University Press, New York, 1991).

47. Haken, H., Brain Dynamics: An Introduction to Models and Simulations (Springer Science & Business Media, 2007).

48. Busciglio, J., Lorenzo, A., & Yankner, B. A. (1992). Methodological variables in the assessment of beta amyloid neurotoxicity. *Neurobiology of Aging*, **13**(5), 609-612.

49. Su, J. H., Cummings, B. J., & Cotman, C. W. (1993). Identification and distribution of axonal

dystrophic neurites in Alzheimer's disease. *Brain Research*, **625**(2), 228-237.

50. Busciglio, J., Hartmann, H., Lorenzo, A., Wong, C., Baumann, K., Sommer, B., et al., (1997). Neuronal localization of presenilin-1 and association with amyloid plaques and neurofibrillary tangles in Alzheimer's disease. *Journal of Neuroscience*, **17**(13), 5101-5107.

51. Selkoe, D. J. (2001). Alzheimer's disease: genes, proteins, and therapy. *Physiological Reviews* **81**(2), 741-766.

52. Grace, E. A., Rabiner, C. A., & Busciglio, J. (2002). Characterization of neuronal dystrophy induced by fibrillar amyloid β: implications for Alzheimer's disease. *Neuroscience*, **114**(1), 265-273.

53. Serrano-Pozo, A., Frosch, M. P., Masliah, E., & Hyman, B. T. (2011). Neuropathological alterations in Alzheimer disease. *Cold Spring Harbor Perspectives in Medicine*, **1**(1), a006189.

54. Caserta, F., Stanley, H. E., Eldred, W. D., Daccord, G., Hausman, R. E., & Nittmann, J. (1990). Physical mechanisms underlying neurite outgrowth: a quantitative analysis of neuronal shape. *Physical Review Letters*, **64**(1), 95.

55. Van Veen, M., & Van Pelt, J. (1992). A model for outgrowth of branching neurites. *Journal of Theoretical Biology*, **159**(1), 1-23.

56. Kiddie, G., McLean, D., Van Ooyen, A., & Graham, B. (2005). Biologically plausible models of neurite outgrowth. *Progress in Brain Research*, **147**, 67-80.

57. Graham, B. P., & Van Ooyen, A. (2006). Mathematical modelling and numerical simulation of the morphological development of neurons. *BMC neuroscience*, **7**(1), 1-12.

58. Meijering, E., Jacob, M., Sarria, J. C., Steiner, P., Hirling, H., & Unser, E. M. (2004). Design and validation of a tool for neurite tracing and analysis in fluorescence microscopy images. *Cytometry Part A: the journal of the International Society for Analytical Cytology*, **58**(2), 167-176.

59. Peng, C. K., Havlin, S., Stanley, H. E., & Goldberger, A. L. (1995). Quantification of scaling exponents and crossover phenomena in nonstationary heartbeat time series. *Chaos: an*

interdisciplinary journal of nonlinear science, **5**(1), 82-87.

60. Peng, C. K., Havlin, S., Hausdorff, J. M., Mietus, J. E., Stanley, H. E., & Goldberger, A. (1995). Fractal mechanisms and heart rate dynamics: long-range correlations and their breakdown with disease. *Journal of electrocardiology*, **28**, 59-65.

61. Govindan, R. B., Wilson, J. D., Preißl, H., Eswaran, H., Campbell, J. Q., & Lowery, C. L. (2007). Detrended fluctuation analysis of short datasets: an application to fetal cardiac data. *Physica D: Nonlinear Phenomena*, **226**(1), 23-31.

62. Grech, D., & Mazur, Z. (2013). On the scaling ranges of detrended fluctuation analysis for long-term memory correlated short series of data. *Physica A: Statistical Mechanics and its Applications*, **392**(10), 2384-2397.

63. Thom, R. (1969). Topological models in biology. *Topology*, **8**(3), 313-335.

64. Thom, R. Structural Stability and Morphogenesis. (W. A. Benjamin, 1975).

65. Blum, H. (1973). Biological shape and visual science (Part I). *Journal of Theoretical Biology*, **38**(2), 205-287.

66. Shibasaki, Y., & Saito, M. (2021). Non-equilibrium entropy and irreversibility in generalized stochastic Loewner evolution from an information-theoretic perspective. *Entropy*, **23**(9), 1098.

67. Oksendal, B. Stochastic differential equations: an introduction with applications. (Springer Science & Business Media, 2013).

68. Falasco, G., Barkai, E., & Baiesi, M. (2022). Generalized virial equation for nonlinear multiplicative Langevin dynamics: Application to laser-cooled atoms. *Physical Review E*, **105**(2), 024143.

69. Fa, K. S. (2003). Linear Langevin equation with time-dependent drift and multiplicative noise term: exact study. *Chemical Physics*, **287**(1-2), 1-5.

70. Lillo, F., & Mantegna, R. N. (2000). Drift-controlled anomalous diffusion: A solvable Gaussian

model. *Physical Review E*, **61**(5), R4675.

71. Marconi, U. M. B., Puglisi, A., Rondoni, L., & Vulpiani, A. (2008). Fluctuation–dissipation: response theory in statistical physics. *Physics Reports*, **461**(4-6), 111-195.

72. Andersen, P. B. (1994). The semiotics of autopoiesis. A catastrophe-theoretic approach. *Cybernetics & Human Knowing*, **2**(4), 17-38.